Deep-Ocean Tides in the South-West Indian Ocean: Comparing Deep-Sea Pressure to Satellite Data

Leo R. M. Maas, Borja Aguiar-González and Leandro Ponsoni

Introduction

Tides have been known to humanity for thousands of years [6]. This knowledge was based on coastal observations of sea surface elevation and associated currents. It was not until the seventeenth century that tides were perceived as very long surface gravity waves that propagate not only along ocean boundaries but that also cross oceans [19]. Observations on the coherent nature of tides, over scales of many hundreds of kilometers or more, started in the nineteenth century [42]. These observations were fraught with surprise, as the tidal field in the North Sea turned out to be much more complex than expected. Its spatial amplitude and phase pattern could be rationalized only by anticipating the existence of amphidromic points: phase singularities at nodal points where the sea surface elevation field vanishes, and around which crest and troughs rotate [42]. Later, the appearance of amphidromes was recognized to be a generic feature in rotating fluids, owing their existence to the Coriolis force that acts transverse to the current. Amphidromic points are now a standard property in the

L. R. M. Maas (✉)
Institute for Marine and Atmospheric Research Utrecht, Utrecht University, Princetonplein 5, 3584 CC Utrecht, The Netherlands
e-mail: L.R.M.Maas@uu.nl

L. R. M. Maas
NIOZ Royal Netherlands Institute for Sea Research, Texel, The Netherlands

B. Aguiar-González
Department of Ocean Systems Sciences, NIOZ Royal Netherlands Institute for Sea Research, Utrecht University, P.O. Box 59, 1790 AB Den Burg, Texel, The Netherlands
e-mail: aguiar@nioz.nl

L. Ponsoni
Georges Lemaître Centre for Earth and Climate Research (TECLIM), Earth and Life Institute, Université catholique de Louvain, Louvain-la-Neuve, Belgium
e-mail: leandro.ponsoni@uclouvain.be

M. G. Velarde et al. (eds.), *The Ocean in Motion*, Springer Oceanography,
https://doi.org/10.1007/978-3-319-71934-4_12

description of tidal patterns, both in the world oceans as well as in coastal regions. In fact, phase singularities, such as amphidromes, have been found in other settings too: e.g. in the inertial wave patterns that appear in homogeneous-density fluids contained in uniformly-rotating, fully-enclosed cubes [4, 5, 18, 21, 27], as well as in other branches of physics, like quantum mechanics [3].

In theoretical models, the simplest version of an amphidrome is obtained in a tidal channel when two counter-propagating Kelvin waves form nodal points [29, 38]. Amphidromes also appear in semi-analytical models of rotationally-modified surface gravity waves, both in half-infinite channels and in rectangular basins [32, 33, 38], as well as in numerical models of more realistically-shaped basins [15], although they are then mixed with Poincaré waves.

Due to the advent of satellite altimetry, however, spatial patterns of combined Kelvin and Poincaré waves could be directly observed in whole-field measurements of the Ocean [7], albeit at three kilometer resolution along and still more crudely across the satellite track. It revealed that on the open ocean, tides are of small-amplitude, a few decimeter at most, in line with the strength of the tidal forcing. Amplification is restricted to coastal regions, first of all due to the exponential character of Kelvin waves, induced by the Coriolis force, but occurring especially when a bay co-oscillates, as when in resonance with a basin mode [10].

Away from the equator, open ocean tides combine propagating, coastally-trapped Kelvin waves with Poincaré waves. Together these display amphidromic points that are traversed mostly in cyclonic (anti-clockwise) sense in the Northern Hemisphere, and *vice versa* in the Southern Hemisphere. However, at times, ocean tides instead display *sloshing*, and are then dominated by standing Poincaré waves that show a behaviour complementary to that of Kelvin waves, exhibiting off-coastal elevation maxima, betrayed by near-uniform phases. One example for the semidiurnal M2 tide is seen in Fig. 1 in the Mozambique Channel. It has a maximum and nearly uniform phase in the narrows. A more striking example, though, can be found in the central Indian Ocean, where the tidal maximum at 75° E, 19° S lies close to a phase saddle point at 71° E, 9.6° S, the point where *two* 260-degrees-phase-lines cross each other (see star in Fig. 1). The uniformity in phase near this local tidal maximum implies that over a large area the semidiurnal tide simply rises and sinks in unison. Notice the 4 amphidromes surrounding this mid Indian Ocean maximum, some lying actually on land (like on Sri Lanka and Madagascar).

The altimetry-derived barotropic tides are based on the Oregon State University Tidal Inversion Software (OTIS) [12]. In this work, we use the TPX08-ATLAS product, which is provided for 9 tidal constituents (M2, S2, N2, K2, K1, O1, P1, Q1 and M4), with a horizontal resolution of 1/30° (http://volkov.oce.orst.edu/tides), see Table 1, although we will not consider M4 tides here.

What will be relevant for the present study is the behaviour of the tide in the Mozambique Channel, as well as along a transect at 23° S, east of Madagascar, where our instruments are located. Taking a cursory look at these two regions, Fig. 1 shows that we may expect quite different behaviour. In the Mozambique Channel, the semidiurnal M2 tide—usually the strongest tidal component—has a standing character, testified by its near-uniform phase, and an amplified tidal elevation which

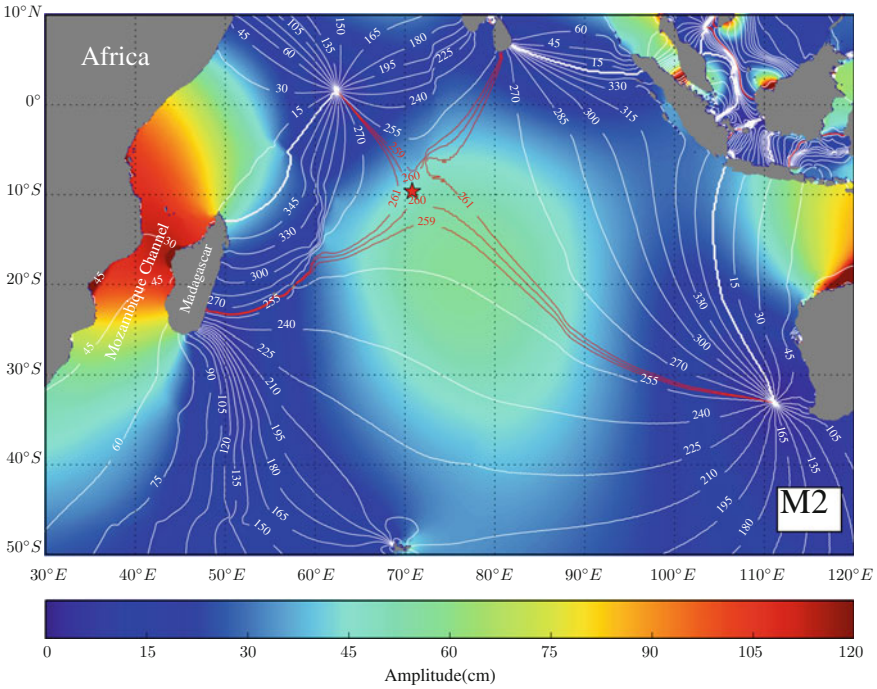

Fig. 1 M2 semidiurnal tidal map obtained from altimetry assimilated by OTIS showing amplitude (color, in cm) and phase with respect to Greenwich Mean Time (GMT) (lines, in °). Tides propagate around amphidromes in the direction of increasing phase. Notice tidal maximum and nearly uniform phase, both in the central Indian Ocean as well as in the Mozambique Channel

Table 1 List of tidal constituents with their corresponding period. Admittance for Mozambique Channel (MC) and East Madagascar (EM) is discussed in section "Coherent Surface and Internal Tides"

Tidal constituent	Period (h)	Admittance MC	Admittance EM
Q1	26.87	1.32	0.47
O1	25.82	1.20	0.28
P1	24.07	0.96	0.25
K1	23.93	0.92	0.26
N2	12.66	4.22	0.61
M2	12.42	5.07	0.51
S2	12	5.88	0.89
K2	11.97	5.85	0.80

reaches a magnitude of about 1.2 m. This betrays a local resonant phenomenon. In stark contrast, East of Madagascar, the M2 tide is close to the nodal point situated on Madagascar. Its surface elevation amplitude is diminished to 10 cm and it shows large phase differences along the coast.

Altimeter observations are assimilated into ocean tide models [37]. These models benefit from the additional constraints provided by the presence of 'sea truth' in the form of deep-ocean tidal observations of pressure. Such contact measurements are useful because altimeter observations do not fully cover the ocean surface. Deformations in the tidal potential, especially near coasts, as well as the presence of coherent yet weak internal tides cause inaccuracies in the determination of surface tidal amplitudes and phases.

For this reason, an effort has previously been put into comparing altimetry-derived tidal elevations to directly-measured tides [34], for which Bottom-Pressure Records (BPRs) have been used. The latter are insensitive to mooring line motions, and may thus provide reliable estimates of the surface tides. However, it turns out that long-term BPRs at depths in excess of 500 m are rare. There appear to be only about 80 deep-ocean pressure records that are at least 100 km apart and that last longer than one year [34]. In the South-West Indian Ocean there are none. Previous shelf and deep-sea bottom pressure measurements [24, 41] have also been used to investigate high-frequency contributions by linear and nonlinear (nonhydrostatic) internal waves, that fall outside the scope of the present investigation.

In the present chapter, we will determine tidal amplitudes and phases of BPRs at moorings deployed at depths in excess of 500 m along two transects in the South-West Indian Ocean, on either side of Madagascar. This region, described in section "Measurement Sites and Instrumentation", is not covered in the previous set of deep-ocean pressure measurements. Altimetry-derived tidal constants for this area are therefore possibly influenced by the presence of the Madagascar and Mozambique coasts and shelves.

The pressure recorders are situated at both a suite of 'bottom locations' (for the purpose of this study defined to be within 75 m from the bottom) as well as at 'mid-depth' sensors within the water column, typically positioned at 500 m below the surface or deeper. Details on these instruments are given in section "Measurement Sites and Instrumentation".

In section "Time Series of Pressure Measurements", all long-term pressure observations are converted to equivalent sea surface displacements and are subjected to a harmonic analysis, yielding tidal amplitudes and phases. Prior to performing the Harmonic Analysis, events showing blow-down of instruments, especially of those deployed far above the bottom, have been eliminated. In section "Coherent Surface and Internal Tides", the harmonic amplitudes and phases derived from BPRs are compared to each other and to altimetry-derived tidal constants. Subsequently, section "Deep Versus Mid-depth Pressure-Measurements of Tides" compares tidal constants derived from BPRs to those obtained from pressure recorders within the water column. In general, within the water column, surface tides explain less of the observed variance in the pressure time series. Part of the tidal variability is due to internal tides. Away from the bottom, amplitudes and phases of the coherent internal

tide—the internal tide that stays phase-locked to the surface tide over the analysed period—can be estimated by subtracting the surface tidal amplitudes and phases, found at BPRs along the same mooring. Incoherent internal tides change amplitude and phase due to changing environmental conditions (stratification and mean-flow structure). Low frequency features as eddies and currents, apart from being responsible for blow-down of mid-water column instruments, also make the determination of long-period tides difficult, which can therefore not be reliably extracted. It is for this reason that we here focus on the eight most prominent diurnal and semidiurnal tidal components only. Conclusions are drawn in section "Conclusions".

Measurement Sites and Instrumentation

The data we use come from two transects in the South-West Indian Ocean:

(1) the narrowest part of the Mozambique Channel (MC), studied in several 'Long-term Ocean Climate Observations' (LOCO) projects, [36, 40], and
(2) East of Madagascar (EM), at 23° S, studied in the 'INdian ATlantic EXchange in present and past climate' (INATEX) project [30, 31].

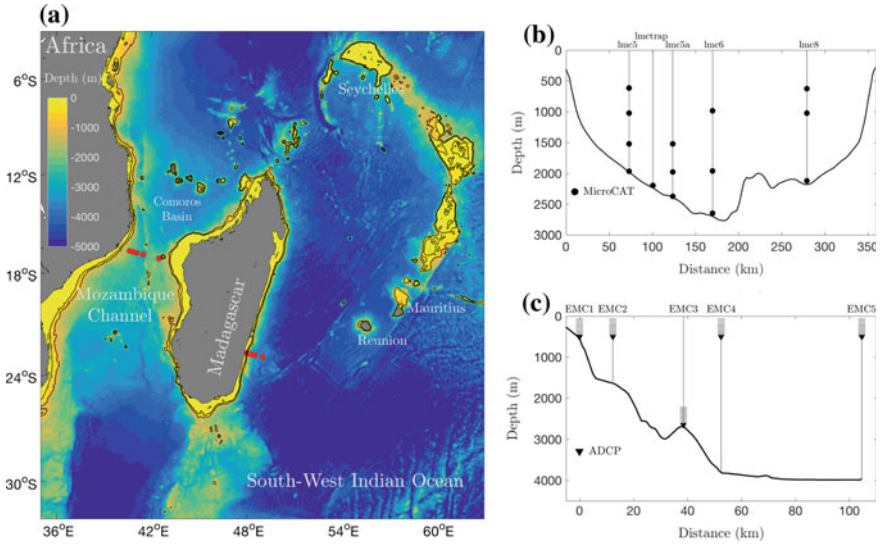

Fig. 2 **a** Bathymetric map (in meters depth) and geographical locations (red dots) of the mooring sites in the narrows of the Mozambique Channel (lmc5, lmctrap, lmc5a, lmc6, lmc8) and off South-East Madagascar (EMC1–EMC5). Detail of the mooring array in **b** the Mozambique Channel and **c** South-East Madagascar

Red dots in Fig. 2a indicate mooring locations in these two regions. Instruments on the moorings provide long-term records of velocity, pressure and hydrographic data. Previous analysis of MC data concerned long-term velocity and temperature records (instruments not shown in Fig. 2b). These were dominated by low-frequency variations due to the yearly, southward passage of four to seven MC-wide eddies [40]. These eddies seem to match the width of the Channel in size but are most pronounced on the Western side and could as well be interpreted as cross-channel propagating Rossby waves [13]. The velocity records also showed evidence of the persistent presence of highly intermittent internal tides with currents ranging from a few up to 10 cm/s [23].

East of Madagascar, the dominant motion is marked by a western boundary current, the East Madagascar Current (EMC). This along-coastal, southward-directed mean-flow eventually feeds the Agulhas Currents further south. At 23° S a steady train of westward propagating cyclones and anticyclones drive the EMC's main band of variability [31].

Here, we focus on data from pressure recording instruments, carried by SBE37-SM MicroCATs in the Mozambique Channel and by upward-looking Acoustic Doppler Current Profilers (ADCPs—RDI Workhorse Long Ranger 75 kHz) off Eastern Madagascar. The positions of these instruments on the mooring lines are indicated in Fig. 2b and c and in Tables 2 and 3.

Tidal amplitudes and phases are obtained from observed pressure time series with T_TIDE, a Harmonic Analysis package [28]. Using a least-squares method, this package determines amplitudes and phases for a given number of tidal constituents whose frequencies are known from celestial mechanics. Here we pay attention to the restricted set of frequencies listed in Table 1. We exclude the very long period tides (such as the Solar Semi-Annual, SSA, and monthly, MSM), as well as higher harmonics, such as M4, and will concentrate on the most prominent diurnal and semidiurnal frequencies, such as M2.

To eliminate the influence of low-frequency phenomena and associated blow-downs the pressure data were handled in the following way: (1) The mean pressure is subtracted. (2) Resulting pressures are divided by the product of density, ρ, and acceleration of gravity, g, yielding an equivalent surface 'displacement' time series, where a positive surface elevation is presented as a negative displacement. (3) The resulting displacement series was detrended. (4) A High-Pass (HP) filter was applied. (5) Blow-down events were eliminated to avoid estimating artificially large tidal amplitudes. (6) The resulting (gappy) time series was subjected to Harmonic Analysis, using T_TIDE applied to periods of one year length, attributing its resulting amplitudes and phases to its centre time. (7) To see the slow evolution of harmonic amplitudes and phases, this harmonic analysis was performed over subsequent one year periods, stepping forward by one day at a time, over a period of 9 to 21 months (a procedure that we call Moving T_TIDE, or MT_TIDE).

In step (2) an 'equivalent surface displacement' is defined for the following reason. While we measure pressure, both near the bottom, as well as within the water column, which varies due to hydrostatic effects (weight of fluid column) and non-hydrostatic effects (vertical accelerations), subtracting the mean pressure, its time-

Table 2 Summary of MicroCATs deployed in the narrows of the Mozambique Channel during LOCO 4, LOCO 5 and LOCO 6, and used in this study. See Fig. 2 for details of the instrument mooring design and location

Moor. site Depth (m)	Position	LOCO period	Instrument depth (m)	Meters above bottom	Total days	Dates mm/dd/yy
lmc5 1992 m	16° 38.86 S 40° 36.82 E	LOCO 4	617	1375	647	01/31/08–11/08/09
		LOCO 4	1020	972	613	01/31/08–10/05/09
		LOCO 4	1520	472	647	01/31/08–11/08/09
		LOCO 4	1966	26	647	01/31/08–11/08/09
lmctrap 2241 m	16° 42.40 S 40° 51.06 E	LOCO 5	2200	41	775	12/20/09–02/03/12
lmc5a 2402 m	16° 45.64 S 41° 3.76 E	LOCO 6	1520	882	863	02/06/12–06/18/14
		LOCO 6	1975	427	863	02/06/12–06/18/14
		LOCO 4	2375	27	220	01/31/08–09/07/08
lmc6 2691 m	16° 52.26 S 41° 28.72 E	LOCO 6	985	1706	863	02/06/12–06/18/14
		LOCO 6	1960	731	863	02/06/12–06/18/14
		LOCO 6	2650	41	863	02/06/12–06/18/14
lmc8 2199 m	17° 6.24 S 42° 28.7 E	LOCO 4	625	1574	689	01/31/08–12/20/09
		LOCO 4	1025	1174	689	01/31/08–12/20/09
		LOCO 4	2125	74	689	01/31/08–12/20/09

varying part may *increase* due to (1) suppression of the mooring's buoys and instruments, (2) surface elevations, or (3) isopycnal uplifts (internal waves). We eliminate suppression-related pressure increases, and divide the demeaned pressure by ρg, so as to be able to interpret it as surface displacement where, recall a positive 'displacement' corresponds to a free surface depression. However, these time-varying pressure perturbations may also be due to internal waves (isopycnal displacements). Thus, a given pressure perturbation, interpreted as an *equivalent* surface elevation (or surface displacement), could also be interpreted as an isopycnal displacement, but, due to the much weaker density contrast, of much larger vertical extent.

Table 3 Summary of the ADCPs deployed off South-East Madagascar during the INATEX project. See Fig. 2 for details

Mooring site	Position	Inst. mean depth (m)	Local depth (m)	Total days	Dates mm/dd/yy
EMC1	22° 41.879 S 48° 1.006 E	500	504	909	10/06/10–04/02/13
EMC2	22° 43.484 S 48° 8.013 E	500	1603	924	10/06/10–04/17/13
EMC3	22° 46.950 S 48° 22.860 E	2600	2654	924	10/06/10–04/17/13
EMC4	22° 48.689 S 48° 30.827 E	500	3799	924	10/06/10–04/17/13
EMC5	22° 55.483 S 49° 0.435 E	500	3959	924	10/05/10–04/16/13

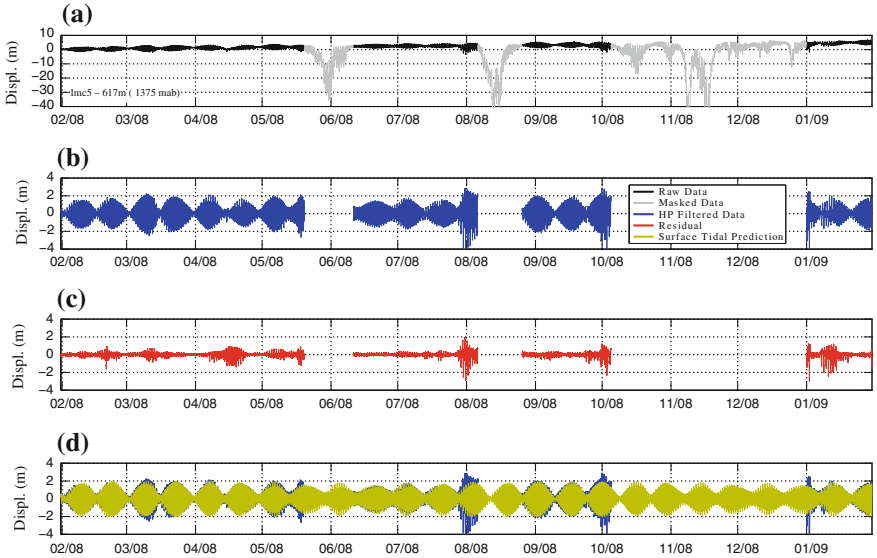

Fig. 3 Time series of pressure, converted to displacement, at lmc5 (at an average depth of 617 m), showing **a** demeaned and detrended time series of vertical displacements, **b** High-Passed filtered data excluding blow-downs, **c** residual field, not captured by Harmonic Analysis, **d** tidally back-predicted field (yellow) superimposed on HP filtered data (blue) and now also covering the gaps. Notice larger scale in (**a**)

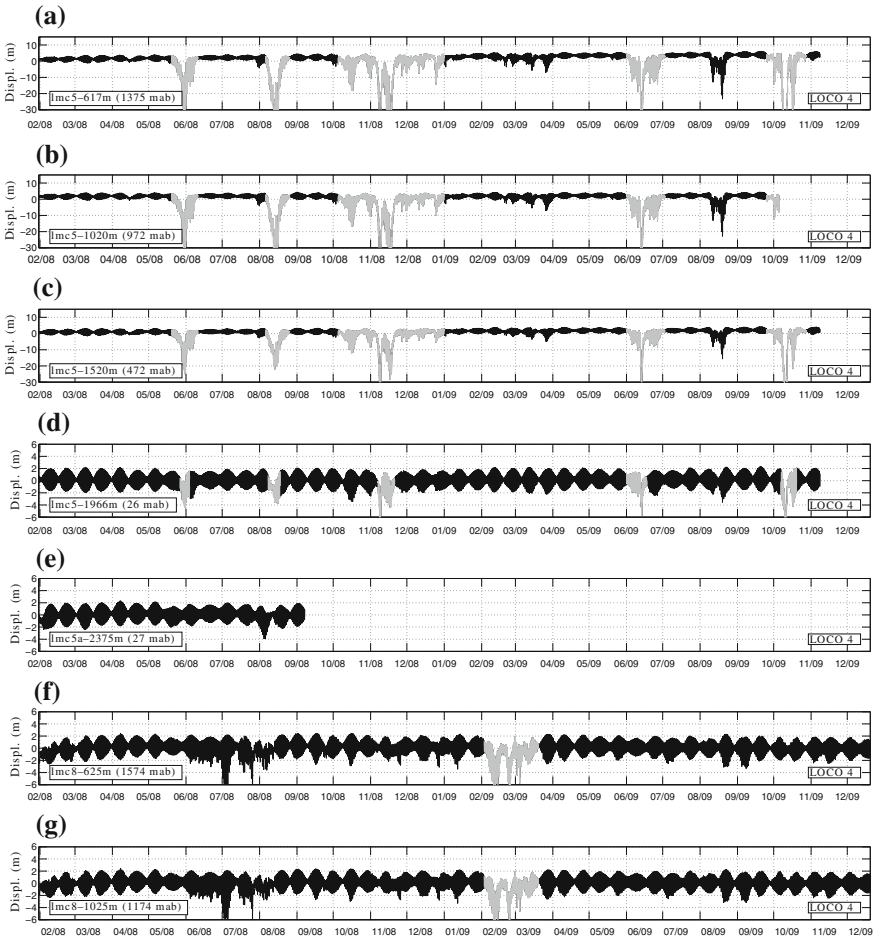

Fig. 4 Time series of equivalent surface displacement as measured by pressure recorders on MicroCATs during **a**–**h** LOCO 4, **i** LOCO 5, **j**–**n** LOCO 6. Time is given in months/year, denoted as mm/yy; November 2009 is e.g. indicated as 11/09. Notice differences in vertical scales and sampling periods. Labels indicate the site name, mean instrument depth and its height in meters-above-bottom (mab). Data in grey are identified as periods affected by blow-down and are, therefore, replaced by NaNs. Further details in Table 2

As High-Pass filter we use a fourth-order Butterworth filter with zero-phase response and cut-off frequency $c^{-1} \times \omega_c$, where $\omega_c = 0.83$ cpd, corresponding to a period of 29.07 h. The band width parameter, $c = 1.25$, was chosen to be narrow enough to capture closely the lowest frequency of interest, ω_c, while being wide enough to avoid filter 'ringing' [1].

An example, illustrating steps (2)–(6), is shown in Fig. 3. Note that the residual signal (red curve) still contains (near) tidal variations, also during periods when

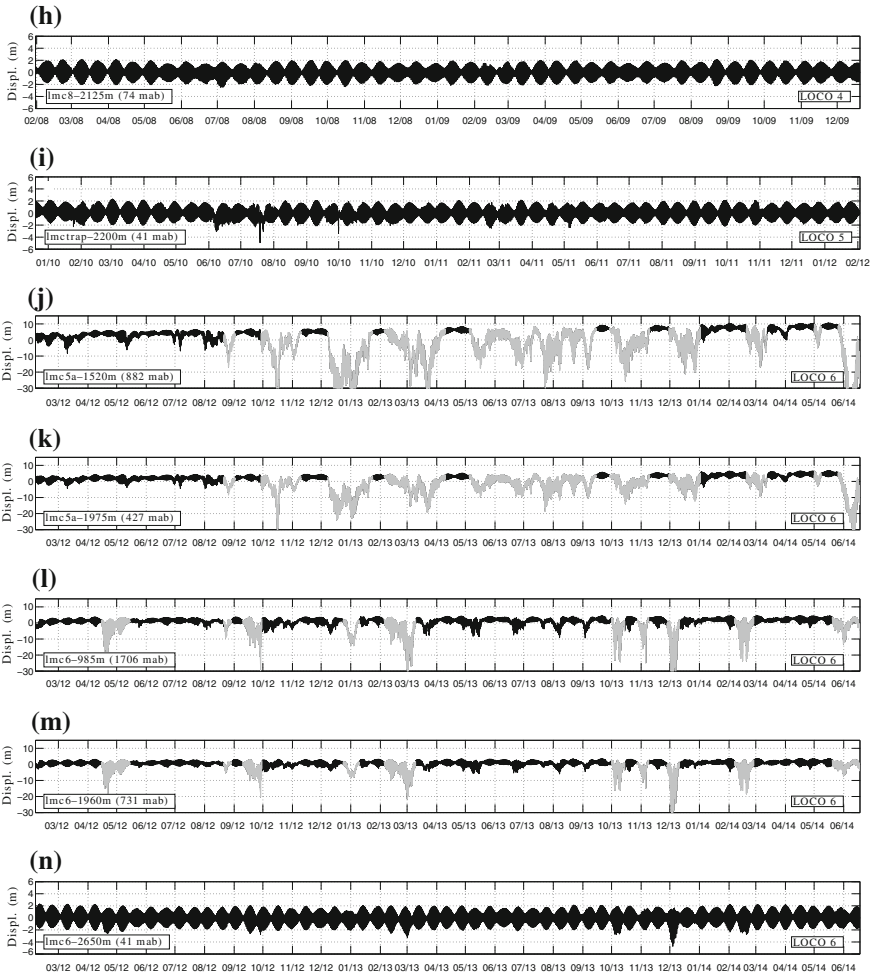

Fig. 4 (continued)

blow-downs do not occur. These come from the spectral cusps, unambiguously representing incoherent internal tides.

In the MC case we visually inspected all time-series, see Fig. 4. We compare neighbouring instruments to elucidate whether the disruption of the 'string of pearls' was actually due to a blow-down event or to some other phenomenon. We were particularly cautious in not removing those phenomena since they introduce natural variability we do not want to remove from our time-series. See for example panel (f) in Fig. 4. Compare events at mooring lmc8 during July and August of 2008 (not marked as NaN) with those during February and March of 2009 (marked as NaN). At first sight one could say both disruptions of the 'string of pearls' are due to a blow-down event, but taking a closer look one realises they are not. The marked events involve

a low-frequency, deep and noticeable excursion while during the non-marked events large-amplitude waves are of high-frequency.

In the EM data, blow-downs were removed by replacing downward displacements in excess of 10 m by NaNs.

Whether large tidal expressions during blow-downs are artificial, resulting from drag forces on buoys exerted by tidal currents superimposed on low-frequency, eddy-related currents, or genuine, expressing internal tides trapped within eddies [2, 17], is not clear and will not be settled here. We note, that HP-filtering also filters out the slow (large-scale) atmospheric pressure contribution to the BPRs. But, as [34] noticed, BPRs may still contain atmospheric tides that would not show up in altimetric measurements, and can be one of the causes for discrepancies between the two.

Time Series of Pressure Measurements

Mozambique Channel

At moorings located along the MC transect in Fig. 2b, Fig. 4 shows time series of both bottom as well as mid-water column pressure recorders. Panels a-h are from LOCO 4 (periods listed in Table 2), panel i from LOCO 5, and panels j-n from LOCO 6. We combine measurements from different LOCO periods to account for the best spatial and temporal coverage of instrumentation across the channel (both along the sea bottom and throughout the water column). The 'string of pearls', visible in all records, represents the spring-neap tidal cycle, produced by superposition of the two dominating surface tidal components, M2 and S2. This supports the notion that amplitude and phase of this tidal interference pattern is about the same for each of these records. Analysis of semidiurnal and diurnal tidal amplitudes and phases, discussed below, will confirm this in more detail.

Most instruments higher up in the water column frequently suffer from large vertical excursions, sometimes reaching apparent displacements of thirty meter or more (see Fig. 4, panels a–c and j–m). Interestingly, despite the long duration of these events (typically lasting a week or longer) these excursions decrease in size with depth. This is odd, as their long duration suggests them to be due to large scale features that should, if these were of a barotropic nature as the surface tide, penetrate throughout the whole water column. The weakening of these vertical displacements with depth suggests these events are instead due to frequent blow-down of buoys, caused by drag forces due to eddy and tide-related currents, that we aim to eliminate. The buoys apparently often fail to keep their mooring lines from pointing straight upwards. During previous observational periods in MC, tilt sensors indeed revealed tilts of over 30° that were moreover tidally modulated with another 5° [23]. Even BPRs sometimes suffer from vertical displacements of 6 m or more that are obviously not produced by surface elevations (see Fig. 4d).

Recall that the displacements defined above, present scaled pressure perturbations that can have different origins. BPRs, however, are not (or very marginally) subject to blow-downs and the interpretation of pressure variations as being due to surface tidal displacements is unambiguous, although we need to remember that an upward sea surface elevation corresponds to a negative displacement. As Fig. 4f–h show, blow-downs seem to be nearly absent at all depths on the most Eastern mooring, lmc8. Together with the bottom-pressure records from two other periods

Table 4 Mean and standard deviation of the variance of the total HP-filtered signal, the tidal signal, and the percent variance explained by the tides predicted from harmonic analyses of MC pressure sensor measurements. Values were computed by averaging all estimates from MT_TIDE. The standard deviation for each estimate is also indicated. Notice that the BPR at lmc5a lasts only seven months making it impossible to establish the evolution of its amplitude and phase. Recall that the mean and trend were removed before the harmonic analysis

Mooring site – Instrument depth (m) Meters above bottom (mab)	Total Var. (m^2)	Tidal Var. (m^2)	Tidal Var. (%)
lmc5 – 617 m (1375 mab)	1.4369 ± 0.3655	1.1491 ± 0.1711	81.9529
lmc5 – 1020 m (972 mab)	1.2545 ± 0.2763	1.0681 ± 0.1425	86.5204
lmc5 – 1520 m (472 mab)	1.0815 ± 0.1708	0.9809 ± 0.0986	91.4791
lmc5 – 1966 m (26 mab)	0.8823 ± 0.0100	0.8744 ± 0.0097	99.1022
lmctrap – 2200 m (41 mab)	0.7923 ± 0.0106	0.7710 ± 0.0166	97.3134
lmc5a – 1520 m (882 mab)	1.2189 ± 0.2256	1.0639 ± 0.1546	88.3847
lmc5a – 1975 m (427 mab)	1.0412 ± 0.1270	0.9825 ± 0.1076	94.6039
lmc5a – 2375 m (27 mab)	0.8669	0.8604	99.2438
lmc6 – 985 m (1706 mab)	1.5220 ± 0.1595	1.0794 ± 0.1243	70.8571
lmc6 – 1960 m (731 mab)	1.2055 ± 0.0929	1.0133 ± 0.0802	84.0482
lmc6 – 2650 m (41 mab)	0.9243 ± 0.0165	0.9160 ± 0.0132	99.1108
lmc8 – 625 m (1574 mab)	0.9321 ± 0.0546	0.8158 ± 0.0239	87.7736
lmc8 – 1025 m (1174 mab)	0.9160 ± 0.0474	0.8206 ± 0.0224	89.7537
lmc8 – 2125 m (74 mab)	0.8293 ± 0.0073	0.8236 ± 0.0076	99.3154

(panels d, e, i and n) these measurements confirm the dominance of surface tides in the time-varying pressure field. At other locations, however, mid-water column pressure signals frequently suffer from severe blow-down. This is a common feature for pressure measurements within the water column, and for this reason often only BPRs are used in the validation of altimetry-derived harmonic constants [34]. In section "Coherent Surface and Internal Tides", we will therefore first look at BPRs, but, since we also want to analyse pressure records higher up in the water column (section "Deep Versus Mid-depth Pressure-Measurements of Tides"), we subject all our measurements to the following procedure.

The amplitudes and phases resulting from MT_TIDE are assigned to the central time within each one-year time interval. Those of the most important semidiurnal and diurnal components are discussed in the next sections. The tidal variance estimate, obtained by averaging the variance of subsequent T_TIDE analyses, and its relative contribution to the total HP-variance, are shown in Table 4. The total and tidal variance are all O (1 m^2). For all moorings, a weak increase of the total HP-variance with height above the bottom is noticed. Except for the most Eastern mooring, lmc8, the tidal variance also increases with height above the bottom. This may be related to the stronger presence of coherent internal tides higher up in the water column, while being weaker or absent in the bottom boundary layer. Yet, the relative contribution of the tides to the total variance always decreases towards the surface. This may be attributed to the stronger (oceanic and atmospheric) mesoscale activity near the surface, introducing more phenomena influencing the pressure variability. Note that the tidal variance in Table 4 that T_TIDE computes for each one year period is based on many more (High-Passed) tidal components than those listed in Table 1, including higher harmonics, the so-called shallow water tides [28]. But in the following we will focus on just the major eight (semi)diurnal components.

East Madagascar

East of Madagascar, tides are much weaker than in the Mozambique Channel, at least near the bottom where they measure free surface displacements of O(10 cm) for the main tidal component, M2. Figure 5a, c show BPR (black line), tidal back-prediction (grey) and residual (red) at moorings EMC1 and EMC3, respectively (see Table 3). Notice that at these two instruments the total apparent surface displacement is restricted to about 1 m. The other three instruments in Fig. 5b, d, e, all far above the bottom, indicate unrealistically large vertical excursions that are a hundred times larger (notice the difference in scale). These are obviously due to mooring motions, resulting in occasional blow-down.

Harmonic Analysis of the BPRs at moorings EMC1 and EMC3 shows that the tides give a modest, yet genuinely tidal contribution of O(8–32%) to the total variance (Table 5). Indeed, this estimate of tidal variance looks reliable in Fig. 5, when comparing the tidal string of pearls (grey) to the variance carried by the residual (red). As to the question *why* these values are so low (compared to those in MC),

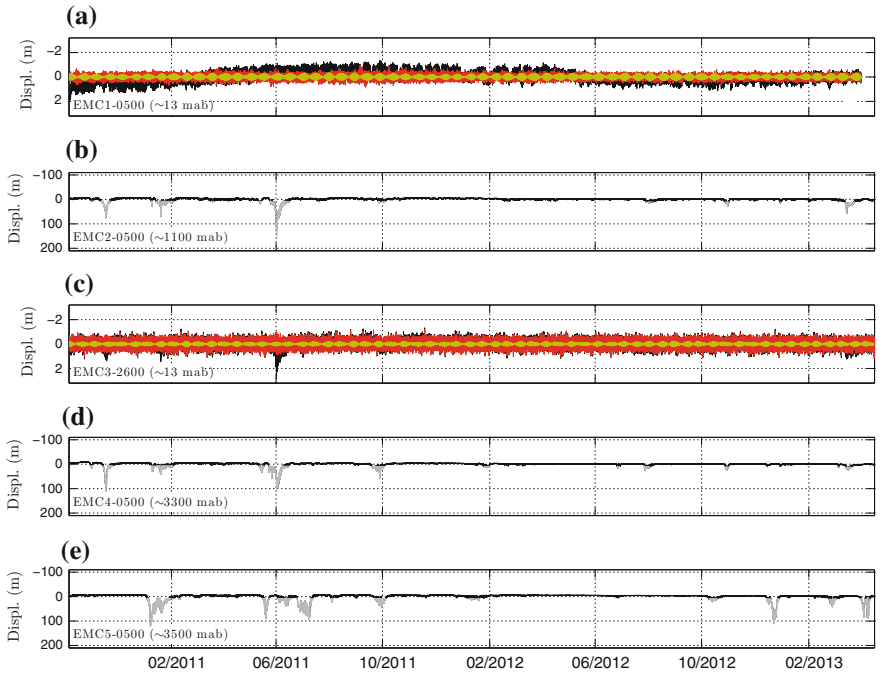

Fig. 5 EM time series (sampled from Oct/2010 to Apr/2013) converted to displacements (black line). Grey and yellow lines in panels **a** and **c** represent the tidal prediction and residual time series, respectively

Table 5 As Table 4 for the EM time series

Mooring site	Total Var. (cm^2)	Tidal Var. (cm^2)	% Tide
EMC1	0.048 ± 0.007	0.015 ± 0.002	31.97 ± 1.16
EMC2	1.372 ± 0.369	0.298 ± 0.090	21.80 ± 3.15
EMC3	0.083 ± 0.001	0.007 ± 0.001	8.54 ± 0.78
EMC4	1.103 ± 0.441	0.299 ± 0.136	26.58 ± 1.95
EMC5	2.317 ± 1.062	0.370 ± 0.205	15.47 ± 3.01

we are still guessing. Fourier spectra, show that after removal of the coherent tides there are still energetic peaks present in the cusps, surrounding the main tidal peaks. But, inspection of time series of BPRs clearly shows that EMC3 has many more supra-tidal oscillations than EMC1, which are corroborated by a higher level of the HF part of the Fourier spectrum (not shown). Whether this reflects the presence of shorter period surface waves, possibly related to the hill at which EMC3 is situated (see Fig. 2c), higher instrumental noise, internal waves, or has some other cause is not clear.

For the other instruments, tidal variance contributes a similar amount to the total variance, O(15–25%), but this does not necessarily represent surface or coherent internal tides. As testified by the much larger *relative* standard deviations in Table 5 of all variance estimates at EMC2, 4 and 5 when compared to those of the BPRs at EMC1 and 3, intermittent internal tides overshadow the surface and coherent internal tides. We will come back to this in section "Deep Versus Mid-depth Pressure-Measurements of Tides".

Coherent Surface and Internal Tides

Harmonic amplitudes and phases of surface tides should not depend on the particular observational time window from which they are determined (provided the observational period is long enough). By definition also the coherent internal tides have stable amplitudes and phases, albeit differing from those associated with the surface tide. Amplitude and phase stability can be used as a criterion to distinguish genuine from 'false' tidal signals (i.e. pressure variations due to tidal-current induced depression of instruments), or on a more positive note, can be used to separate the combined surface and coherent internal tides from incoherent internal tides. The moving version of the harmonic analysis performed by T_TIDE (MT_TIDE) allows us to make this separation.

Mozambique Channel Harmonic Constants

The results of running MT_TIDE for the Mozambique Channel pressure records are presented in Figs. 6 and 7 for semidiurnal and diurnal frequencies, respectively. The fluctuations in, especially amplitude, that occur for pressure records within the water column will be discussed in section "Deep Versus Mid-depth Pressure-Measurements of Tides", although it should be noticed here that tidal amplitudes are not necessarily always larger higher up in the water column, compared to the very stable bottom amplitudes. See for instance in Fig. 6 the M2 amplitude at lmc8. Phases are very stable at nearly all locations, amplitudes only near the bottom. It is significant that the least stable estimates and the largest M2 tidal amplitudes are found at the mid-channel mooring lmc5, especially at the pressure sensors that are highest above the bottom. At the three 'bottom' locations (less than 75 m away from the bottom), M2 amplitudes are around 113 cm. Phase differences are generally small. For M2 the phase centers around 37°. For the second most important component, S2, the amplitude is about 60 cm, and its phase about 79°. The other two semidiurnal components, N2 and K2, both reach amplitudes of O (17 cm).

Diurnal components (Fig. 7) also have quite stable amplitudes and phases. Amplitudes of O (2–7 cm) are smaller than those of the semidiurnal tides. The spreading in phase estimates is often larger than that of the semidiurnal components. Table 6

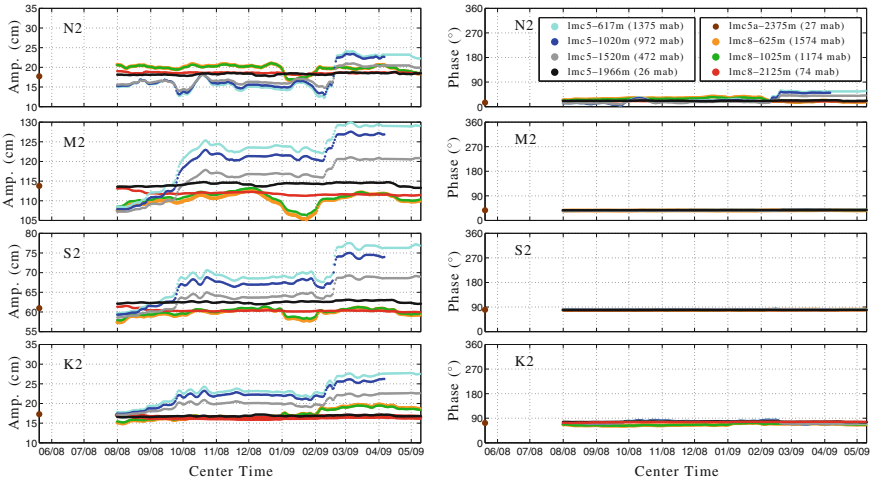

Fig. 6 Amplitudes (left, cm) and phases (right, °) of semidiurnal tidal constituents in MC during LOCO 4 obtained from MT_TIDE. Labels indicate the site name, mean instrument depth, and instrument height in meters-above-bottom (mab). The circle on the left vertical axis indicates the estimates for lmc5a obtained from T_TIDE applied to seven months of data only

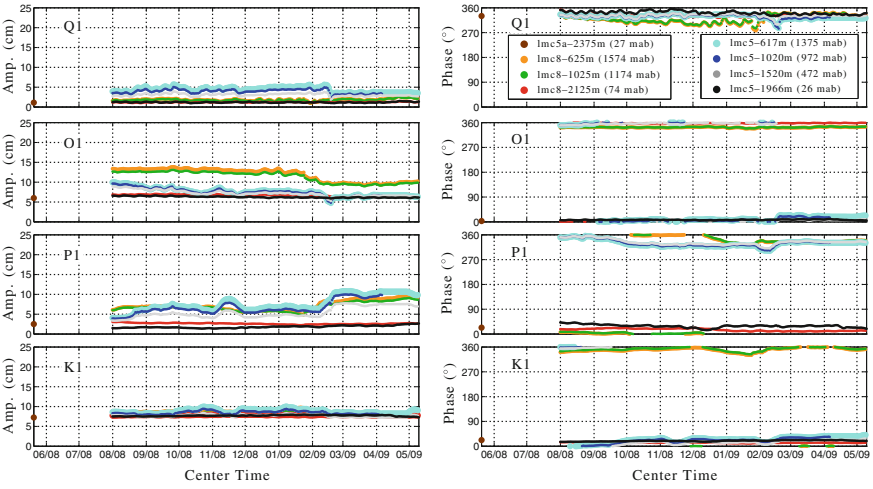

Fig. 7 Same as Fig. 6 for diurnal tidal constituents

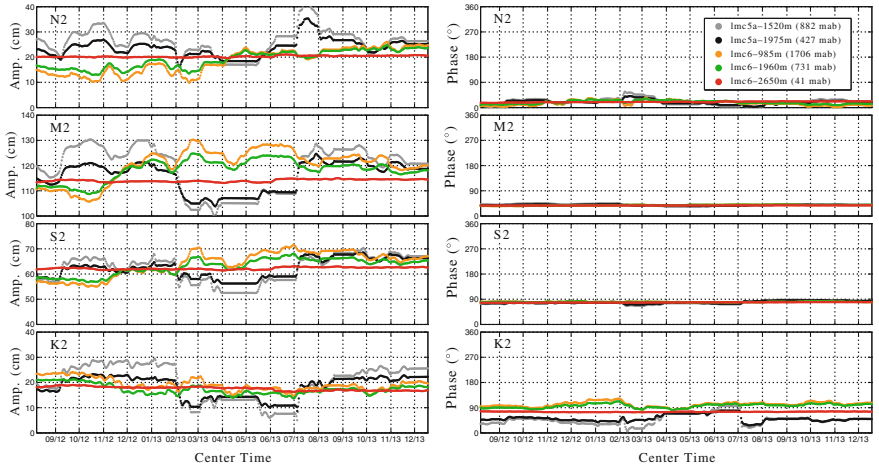

Fig. 8 Amplitudes (left, cm) and phases (right, °) of semidiurnal tidal constituents during LOCO 6 obtained from MT_TIDE. Labels indicate the site name, mean depth, and depth in meters-above-bottom (mab)

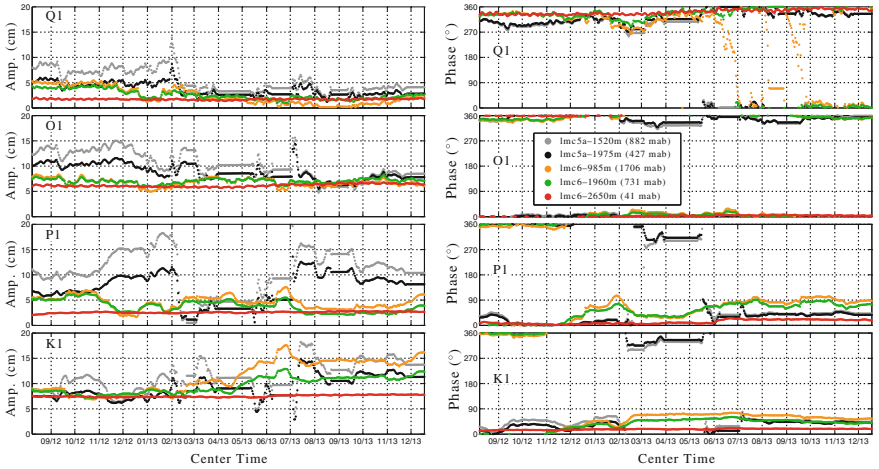

Fig. 9 As Fig. 8 for the diurnal frequencies

summarizes the MT_TIDE average amplitudes, phases and standard deviations of these eight tidal components.

Similar amplitudes and phases during the LOCO 6 period are shown in Figs. 8 and 9. The single BPR that was present in this period, 41 m above the bottom, at lmc6 (red curves), again has very stable tidal amplitudes and phases, in line with those obtained for the LOCO 4 period.

Table 6 Mean amplitude (cm) and phase (°) from MT_TIDE applied to the Mozambique Channel bottom pressure recorders. Instrument deployment height is indicated as meters-above-bottom (mab). Columns are ordered from West to East

Tidal Const.	lmc5–1966 m (26 mab)		lmctrap–2200 m (41 mab)		lmc5a–2375 m (27 mab)		lmc6–2650 m (41 mab)		lmc8–2125 m (74 mab)	
	Amp. (cm)	Phase (°)	Amp. (cm)	Phase (°)	Amp. (cm)	Phase (°)	Amp. (cm)	Phase (°)	Amp. (cm)	Phase (°)
Q1	1.2 ± 0.1	342.6 ± 6.1	1.6 ± 0.2	308.6 ± 13.9	1.1	330.2	1.7 ± 0.1	341.9 ± 8.6	1.2 ± 0.1	332.1 ± 4.7
O1	6.3 ± 0.2	7.2 ± 1.2	7.0 ± 0.2	352.1 ± 4.3	6.0	2.8	6.2 ± 0.3	2.5 ± 2.4	6.7 ± 0.2	358.3 ± 1.0
P1	1.8 ± 0.3	28.6 ± 5.3	3.0 ± 0.4	22.1 ± 7.3	2.5	23.2	2.6 ± 0.1	12.6 ± 7.5	2.6 ± 0.2	15.9 ± 4.4
K1	7.7 ± 0.1	19.5 ± 2	6.0 ± 0.2	349.5 ± 4.9	7.2	22.2	7.5 ± 0.2	17.4 ± 2.0	7.9 ± 0.1	12.5 ± 1.1
N2	18.3 ± 0.2	21.5 ± 0.9	17.1 ± 0.8	15.1 ± 1.4	17.7	14.9	20.3 ± 0.3	20.2 ± 1.6	18.6 ± 0.2	19.8 ± 0.6
M2	114.2 ± 0.4	38 ± 0.3	106.9 ± 0.9	36.4 ± 0.4	113.8	37.3	114.1 ± 0.5	37.7 ± 0.3	111.8 ± 0.4	37.4 ± 0.3
S2	62.5 ± 0.3	79.1 ± 0.2	57.7 ± 0.5	79.2 ± 0.7	61.0	80.0	62.2 ± 0.4	78.7 ± 0.7	60.3 ± 0.3	78.7 ± 0.3
K2	16.8 ± 0.2	77.1 ± 0.6	14.7 ± 0.8	73.3 ± 1.2	17.3	72.7	17.6 ± 0.8	75.3 ± 1.0	16.5 ± 0.2	76.0 ± 1.1

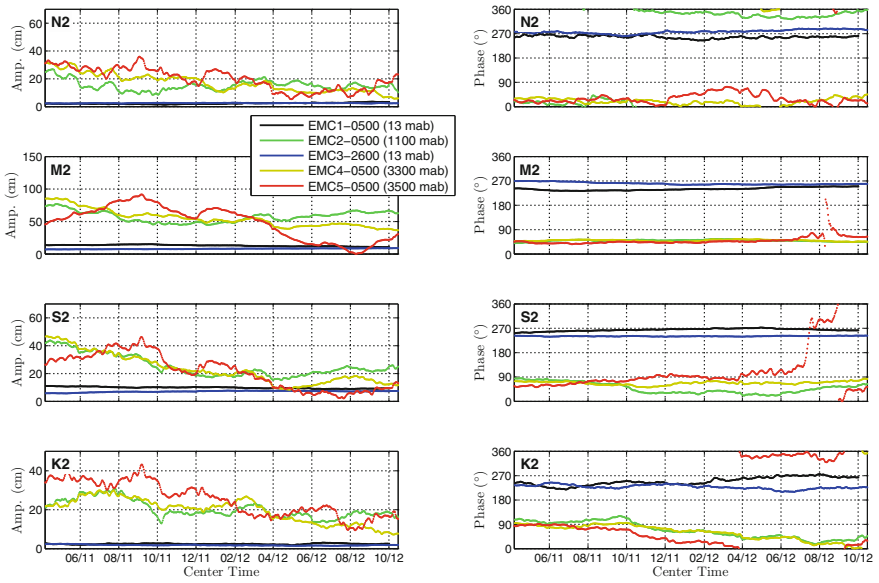

Fig. 10 Amplitudes (left, cm) and phases (right, °) of semidiurnal tidal constituents in EM, obtained from MT_TIDE. Labels indicate the site name and mean depth

East Madagascar Harmonic Constants

The slow-time evolution of semidiurnal amplitudes and phases for the East Madagascar moorings, after standard HP-filtering and blow-down removal, is shown for the four major semidiurnal frequencies in Fig. 10. These panels show that: (1) tidal amplitudes of O (10 cm) and phases are very stable at near-bottom instruments (EMC1 and EMC3), represented by a single average value (Table 7) together with a variance estimate (Table 5), (2) M2 tidal amplitudes at 'mid-depth' (EMC2, 4 and 5) are very high, O (50–100 cm), (3) tidal amplitudes at mid-depth depend on the precise computational interval for which T_TIDE is run—the time around which the one-year time series is centred, (4) for bottom instruments—representative of barotropic tides—phases of all semidiurnal components are nearly the same (approximately 250°), (5) compared to the phase of these BPRs, mid-depth pressure series are often roughly in anti-phase (on average, about 160° phase difference).

Similar observations can be made for the diurnal components, Fig. 11. Phases of bottom instruments (EMC1 and 3, black and blue lines respectively) are again stable despite very small O (1 cm) amplitudes, albeit now showing differences from one diurnal component to the next. Mid-depth instruments at EMC2, 4 and 5 still have very large amplitudes, but phases sometimes change rapidly. Phase changes of 180° (such as that for O1 in September 2012), are likely indicative of the passage of a node of an internal tide's vertical elevation field, that separates rising drom depressing isopycnal surfaces.

Table 7 Mean amplitude (cm) and phase (°) from MT_TIDE applied to the East Madagascar pressure recorders. Notice that recorders at EMC1 and EMC3 represent BPRs, while at the other moorings they are positioned 500 m below the surface. Columns are ordered from West to East

Tidal constituent	EMC1		EMC2		EMC3		EMC4		EMC5	
	Amp. (cm)	Phase (°)	Amp. (cm)	Phase (°)	Amp. (cm)	Phase (°)	Amp. (cm)	Phase (°)	Amp. (cm)	Phase (°)
Q1	0.6 ± 0.2	277.5 ±124.5	7.0 ± 4.1	175.9 ±29.6	0.7 ± 0.1	290.4 ± 11.0	4.3 ± 1.3	245.3 ± 76.0	5.1 ± 2.2	235.4 ± 93.4
O1	1.9 ± 0.6	35.0 ±13.9	4.1 ± 0.9	189.9 ±150.1	2.2 ± 0.1	23.5 ± 3.1	2.6 ± 1.4	133.9 ± 110.5	6.4 ± 2.3	114.4 ± 102.6
P1	1.2 ± 0.1	87.8 ±12.4	4.2 ± 2.8	185.1 ± 70.8	0.5 ± 0.3	98.4 ± 55.9	3.2 ± 1.7	229.5 ± 61.6	10.5 ± 5.7	84.5 ± 85.3
K1	2.7 ± 0.1	101.4 ± 4.1	11.3 ± 2.5	78.7 ± 18.8	2.6 ± 0.4	111.1 ± 7.7	9.3 ± 2.8	73.4 ± 8.1	16.0 ± 5.2	100.0 ± 13.9
N2	2.3 ± 0.5	257.8 ± 5.4	15.2 ± 3.6	233.3 ± 53.6	2.5 ± 0.1	277.2 ± 7.0	17.1 ± 6.5	38.5 ± 76.3	20.0 ± 7.9	34.1 ± 39.8
M2	13.0 ± 1.2	240.5 ± 5.4	57.5 ± 8.4	49.3 ± 3.6	8.0 ± 0.6	260.6 ± 4.5	54.8 ± 13.0	49.9 ± 2.9	48.6 ± 25.9	50.0 ± 17.1
S2	9.9 ± 0.6	264.3 ± 4.6	25.4 ± 7.7	49.0 ± 19.7	7.1 ± 0.5	240.9 ± 1.1	23.1 ± 10.5	67.8 ± 6.5	21.4 ± 12.4	99.7 ± 66.0
K2	2.4 ± 0.3	249.4 ± 14.9	20.3 ± 4.5	67.7 ± 30.1	1.8 ± 0.3	228.3 ± 7.9	19.6 ± 6.3	65.3 ± 47.4	25.3 ± 8.7	138.0 ± 135.1

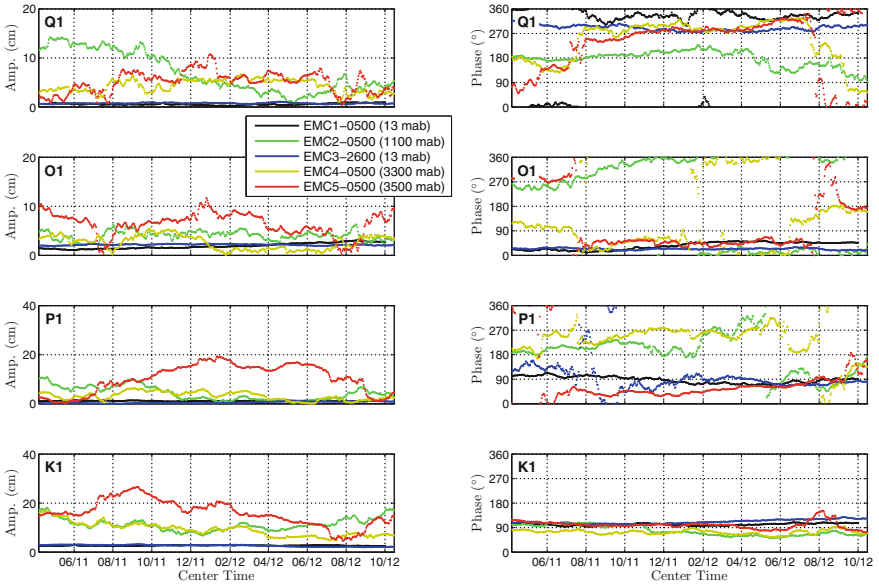

Fig. 11 Same as Fig. 10 for diurnal frequencies

Long-term averages, obtained from MT_TIDE, are shown in Table 7. They show the stability of the BPR-derived tidal amplitudes at EMC1 and 3: a signal-to-noise ratio (SNR), defined by the ratio of standard deviation to amplitude, of O (10%). This contrasts with the SNR for mid water column pressure records at EMC2, 4 and 5, which is O (30–50%). Of course, they also show that bottom pressure fluctuations, converted to surface displacement, have smaller amplitudes than those within the water column, were they again point at the presence of internal tides (see section "Deep Versus Mid-depth Pressure-Measurements of Tides").

Bottom-Pressure Versus Altimetry Derived Tides

The first and third rows of Fig. 12 display diurnal and semidiurnal tidal amplitudes, A, and phases, ϕ, from Table 6 of the five BPRs in MC. These are the amplitude and phases of an equivalent surface elevation field computed from the BPRs which are here presented in terms of the real and imaginary components $A(\cos\phi, \sin\phi)$ of the complex vectors $A\exp(i\phi)$. Similar 'harmonic vectors', obtained from satellite altimetry (OTIS), are shown in the second and fourth rows.

The comparison between BPRs and altimetry (OTIS) vectors in the Mozambique Channel, where tides are large, is excellent, especially for the semidiurnal components (last two rows). The difference vectors are O (5%) in magnitude compared to those of the BPRs, for which reason, in section "Deep Versus Mid-depth

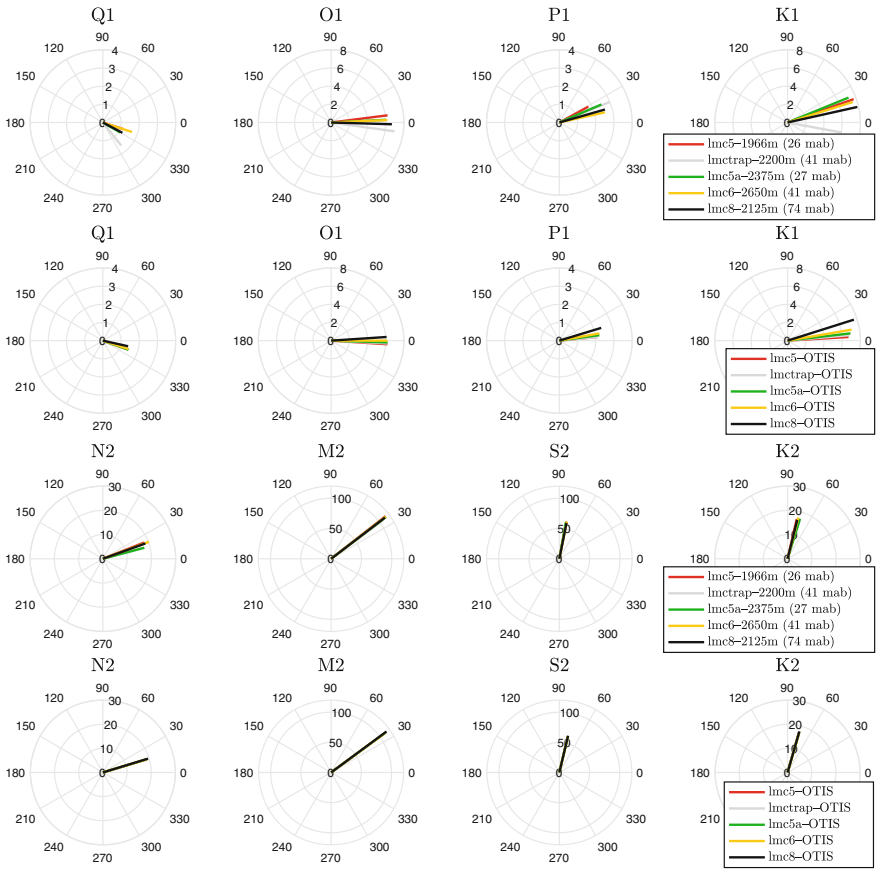

Fig. 12 Polar plots showing horizontal variation of amplitudes (cm) and phases (°) of diurnal (top two rows) and semidiurnal tidal constituents (bottom two rows) in MC as seen from bottom instruments and satellite altimeter (OTIS) data. The legend indicates the site name and mean depth. Notice differences in scale

Pressure-Measurements of Tides", BPR-derived harmonic vectors have been subtracted from those higher up in the water column. We subtract these BPR signals because, as they agree with altimetric tides, we can take them as representative of surface tides. Therefore, its subtraction from harmonic signals obtained from pressure records higher up in the water column leads to the signal of coherent internal tides. Semidiurnal tides appear spatially synchronised, and thus appear as standing waves. The diurnal components (first two rows) show more variations at the bottom. Those derived from altimetry (OTIS) show a clear and consistent eastward phase increase (from lmc5 towards lmc8), and also a slight increase in amplitude. By contrast, the BPRs show in general a slight westward phase propagation, although somewhat more erratic. Especially the bottom pressure recorder at lmctrap behaves, as we shall see later, somewhat differently for most frequencies. Comparing to harmonic

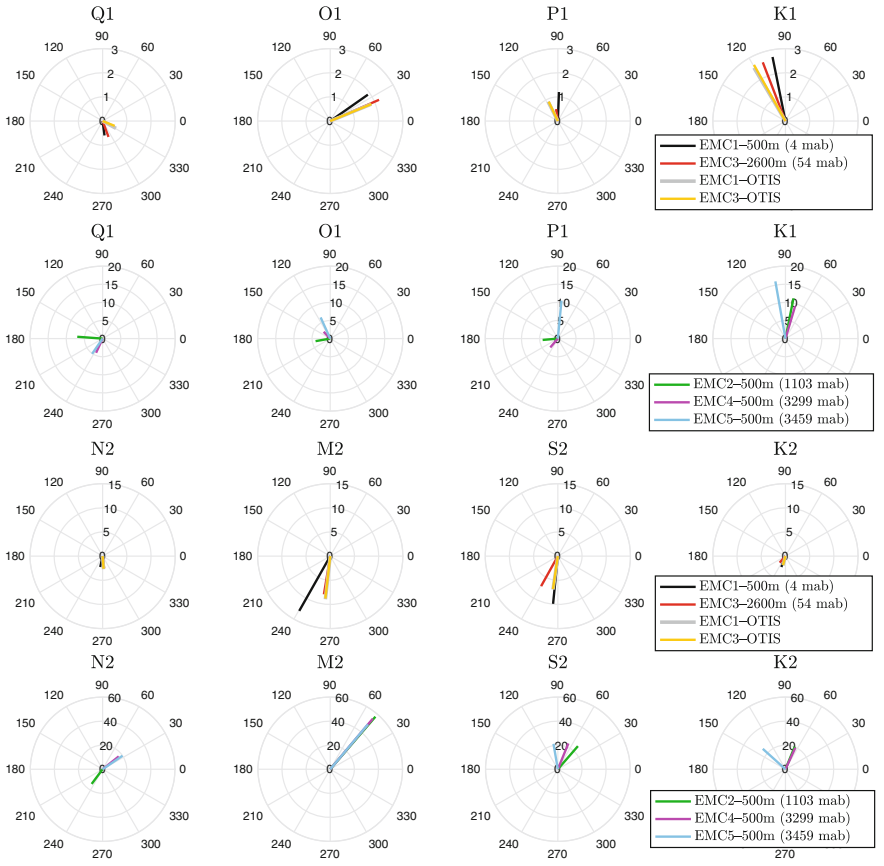

Fig. 13 Amplitudes (cm) and phases (°) of diurnal (top row) and semidiurnal (third row) tidal constituents at sites EMC1 and EMC3 as seen from BPRs and OTIS data. Amplitudes (cm) and phases (°) of diurnal and semidiurnal tidal constituents within the water column, at sites EMC2, EMC4 and EMC5 (second and fourth rows). The legend indicates the site name, mean depth and meters-above-bottom. Note that here polar plots share the same scale only within the same row

vectors at lmctrap during other LOCO periods (and using other pressure sensors—not shown), however, confirms the amplitudes and phases found at lmctrap during LOCO 5, although all seem to differ from those obtained at other MC locations. This may bear perhaps evidence of a relatively strong coherent internal diurnal tide that varies over shorter spatial scales than the forcing.

On the transect East of Madagascar, differences of the BPR-derived semidiurnal tides with the altimetric vectors, shown in the third row of Fig. 13, are larger than in MC, possibly because the background, low-frequency fields are relatively stronger and hence the determination of tidal amplitudes and phases less accurate. At EMC1, the OTIS magnitude of the M2 tide differs by O (50%) of that in bottom pressure. The spatial uniformity of the altimetry-derived harmonic constants in EM, that was

mentioned above, may however have been artificial, due to the extrapolation applied to altimetry-derived tidal constants on approach of the shoreline. Coastal proximity inhibits direct satellite altimeter measurements of surface elevations. BPRs show a decrease of surface tidal amplitude with increasing distance to the coast (compare EMC1 to EMC3) of the largest two semidiurnal frequencies (M2 and S2). This is in line with their presence as a Kelvin wave, trapped along the East Madagascar slope, which is expected to propagate northwards.

East of Madagascar, surface diurnal tides shown by BPRs in the first row of Fig. 13 reach amplitudes of O (1–3 cm) and compare well with altimetry derived (OTIS) harmonic vectors. The harmonic vectors at the other, mid-water column pressure sensors, however, are all much larger than those at the bottom, indicating their presence as a strong coherent diurnal internal tide that will be further discussed in section "Deep Versus Mid-depth Pressure-Measurements of Tides".

Credo of Smoothness

In the open ocean and in coastal regions, tides represent the response to body or boundary forces, respectively. In the open ocean, tides are due to the gravitational attraction by sun and moon, modulated by the motion of these celestial bodies, together with the motion and rotation of the earth [29]. Coastal regions (and inland seas and lakes) are too small to be able to respond to tidal forces directly. Coastal tides result due to the tides present at their ocean boundaries, via co-oscillation [10, 14]. Of course, the nature of this response does not only depend on the strength with which tides are present in the tidal potential or at the sea's boundary. Tidal response also depends on geometrical aspects of ocean or coastal basins, which may lead to tidal amplification when resonating with a basin's eigenfrequency, or to its suppression due to choking when in anti-resonance [20, 39]. Viewing the ocean or coastal response to tidal forcing as being determined mainly by the proximity of any of the tidal frequencies to any of the eigenfrequencies of these fluid basins, a certain similarity in the spatial distribution of tides of nearly similar frequency should not come as a surprise. This view was epitomized in the catchy phrase 'credo of smoothness' [26] and is clearly born out in the tidal altimetry fields, both for the semidiurnal and diurnal frequency bands, see Figs. 14 and 15.

At each tidal frequency, the response of the ocean to tidal forcing is given by an amplitude ratio and a phase difference between its locally observed elevation amplitude and Greenwich phase with those present in the tidal potential. Viewing the response of the ocean to tidal forcing as that of an oddly-shaped, damped mechanical resonator, one expects to see grossly similar features for slightly differing tidal frequencies, frictional effects smoothing out any sharp changes. During passage of such a resonance, 180 degree phase changes may still occur, but not abruptly. Looking at

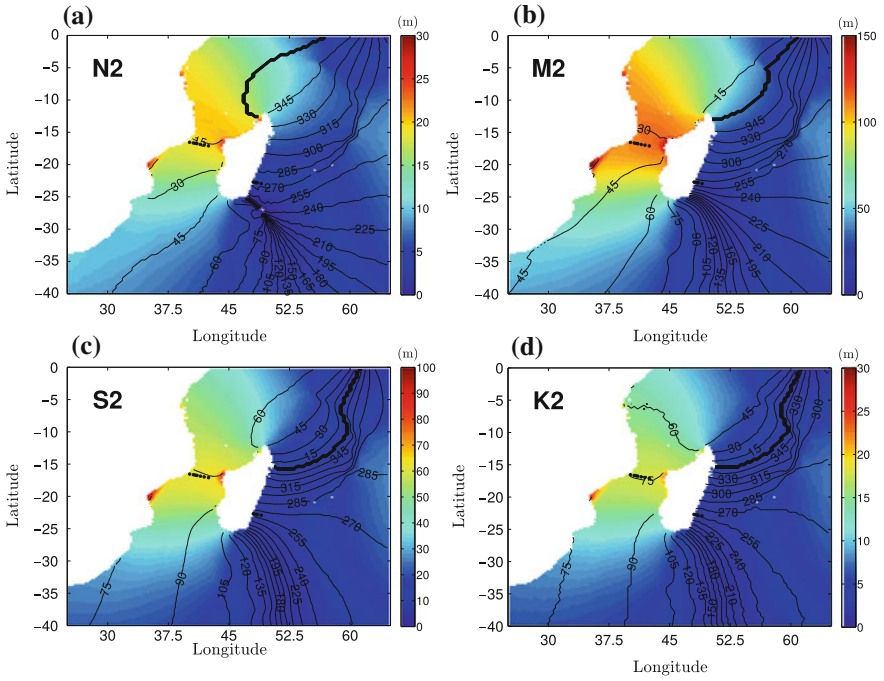

Fig. 14 Spatial amplitude (cm) and phase (°) pattern in the South-West Indian Ocean determined from OTIS by means of satellite altimetry data for semidiurnal tidal components. Mooring locations are indicated by dots

the altimetry-derived amplitudes and phases, Figs. 14 and 15, it is indeed striking to see the resemblance of the amplitude and phase distributions of the four semidiurnal tidal frequencies considered. The pressure observations, presented here, fully support these findings, except that they show that in the vicinity of Madagascar, a Kelvin wave enhancement may take place that may not be directly visible in the altimetry-derived East Madagascar amplitude fields.

By contrast, the tide in the Mozambique Channel is nearly uniform in phase, and suggests a local, geometry-induced resonance. Satellite altimetry (Fig. 1) indeed shows the M2-phase to become uniform a little North of the Mozambique Channel transect, at a phase of about 30°.

A time series of observed sea surface elevation, $\zeta(t)$, can be written as a sum, $\zeta = \sum_j Z_j \sin(\Omega_j t + \phi_j)$, of contributions at tidal frequency, Ω_j, of amplitude Z_j and phase ϕ_j. The ability of a particular geographical region to resonate can be measured by computing the admittance, i.e. the ratio of the observed free surface tidal amplitudes, Z_j, at a certain location, to their amplitudes, $\bar{Z}_j$, as present in the tidal potential. Here we ignore the phase shift involved and evaluate this amplitude ratio only. The tidal potential, W, is for over 98% captured by the first non-vanishing, second-degree term, W_2 [29]. In the equations of motion, this potential is usually expressed as an

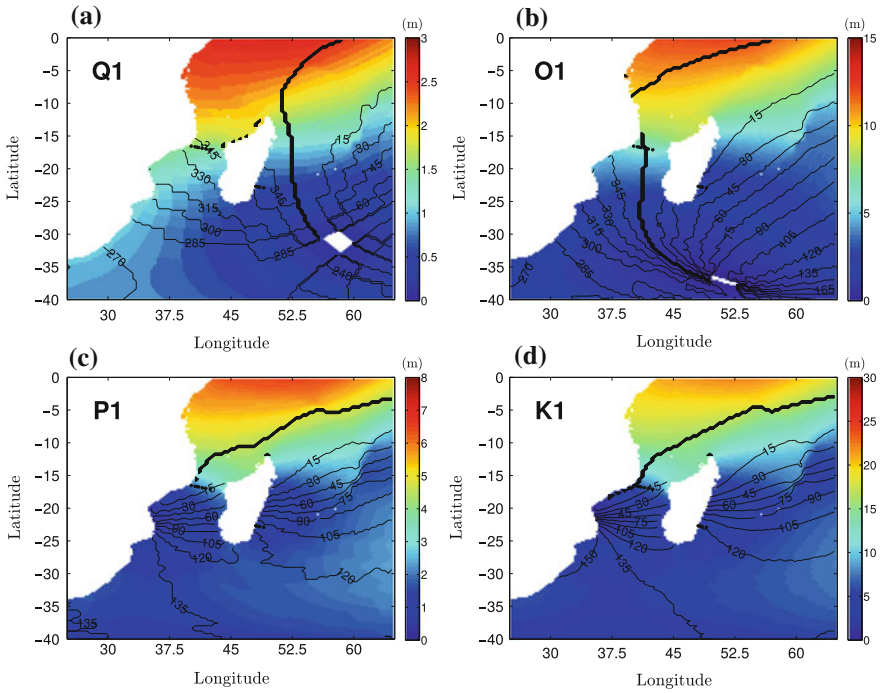

Fig. 15 Same as Fig. 14 for diurnal tidal components

equilibrium sea level, towards which the ocean tends, $\bar{\zeta} \equiv W_2/g$. This equilibrium tide is a nonlinear function of space and time, determined by declinations and rotation rates of Earth and celestial body, and their distance. It can likewise be expanded in a Fourier series and, at a certain geographical location, is expressed as the sum over tidal frequencies of a product of functions of latitude θ, $G_i(\theta)$, of diurnal ($i = 1$) and semidiurnal ($i = 2$) origin, the Doodson constant—an overall amplitude factor—a tidal potential coefficient, C_j, and a trigonometric function of time t and phase angle χ_j (dependent on the location's longitude and orbital parameters of moon and sun):

$$\bar{\zeta} = \sum_j \bar{Z}_j \ \sin(\Omega_j t + \chi_j), \ \text{where} \ \ \bar{Z}_j \equiv C_j G_i D/g.$$

Here, the Doodson constant, $D = 3GMR^2/4d^3$, where G denotes the universal gravitational constant, M the mass of the celestial body, R the radius of the earth, and d the distance of the centre of the Earth to the center of the gravitating body. For the moon, the Doodson constant, divided by gravitational acceleration (g), yields $D/g = 26.75$ cm. The latitude functions of diurnal and semidiurnal tides are given by $G_1 = \sin(2\theta)$ and $G_2 = \cos^2\theta$, respectively. Since the Mozambique Channel and East Madagascar transects have fairly uniform tidal

amplitudes each, we take their average values as observed tidal amplitudes, Z_j, in computing their admittance, $Z_j/\bar{Z}_j$. The tidal potential coefficients, C_j, of the eight tidal frequencies Ω_j: (Q1, O1, P1, K1, N2, M2, S2, K2), are given by [29] and read $C_j = (0.072, 0.377, 0.176, 0.530, 0.174, 0.908, 0.423, 0.115)$. With these coefficients, along the transects in the Mozambique Channel ($\theta \approx 16.75°$ S) and East of Madagascar ($\theta \approx 22.90°$ S), the admittance of these tidal components, $Z_j/\bar{Z}_j$, has been determined, shown in the second and third column of Table 1, respectively. Admittances indeed vary fairly smoothly, particularly in the Mozambique Channel where semidiurnal amplitudes are all resonantly amplified, peaking with an amplification factor of about 5.9, at a frequency in between S2 and K2.

The response at the diurnal frequencies in the Mozambique Channel is about the same as in the tidal potential (admittance close to 1), albeit picking up at frequencies below the lowest diurnal frequency considered here, Q1.

The tides derived from BPRs along the transect East of Madagascar are all suppressed compared to their presence in the tidal potential. The semidiurnal components are weak because of the proximity of an amphidromic point close to the transect; the diurnal components vary at a larger scale, and amplify towards the equator.

Deep Versus Mid-depth Pressure-Measurements of Tides

BPRs of tides show harmonic constants to be very stable. This is surprising as internal tides might well be present at the bottom too. These could lead to a modulation of tidal amplitudes and phases. Consider e.g. a two-layer ocean with upper and lower layer depths h_1 and h_2 and corresponding densities ρ_1 and ρ_2, respectively. Then the hydrostatic pressure at the bottom is given by a stationary part $\rho_1 g h_1 + \rho_2 g h_2$ and a variable part due to elevations of free surface, ζ, or interface, η, given by $g\rho_1\zeta + g(\rho_2 - \rho_1)\eta$. Expressed as elevation, by dividing by $g\rho_1$, this perturbation pressure reads $\zeta + \delta\eta$. It shows that pressure perturbations due to large interface elevations $\eta \gg \zeta$ might still be moderate due to weakness of the density contrast, $\delta \equiv \rho_2/\rho_1 - 1 \ll 1$. When the ocean is continuously-stratified, higher internal modal structures may appear within the sea. The net pressure perturbation at the bottom due to internal displacements can then be less than those within the water column as isopycnal elevations at one depth can be compensated by depressions at another. Judging from the near-bottom stability of the tides, internal tides are weak at the bottom either for the above reason, or because their presence is precluded by the presence of a thick bottom boundary layer at the top of which internal waves reflect, higher up in the water column.

Observations from pressure recorders, mounted higher in the water column do show the presence of internal tides. In fact, they often dominate the pressure signal, especially East of Madagascar, see the second and fourth row of Fig. 13, showing amplitudes at intermediate depths four times those found at the bottom. Mooring lmc8, on the East side of Mozambique Channel, is exceptional in showing hardly any

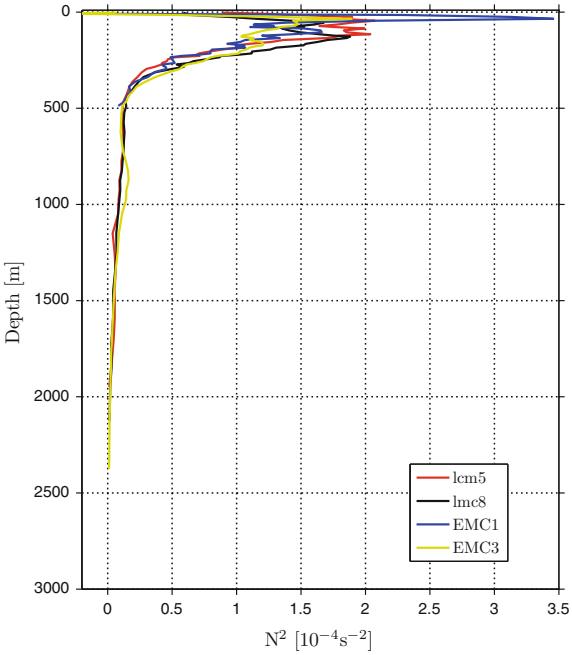

Fig. 16 Buoyancy-squared profiles obtained from CARS09 for Mozambique Channel (lmc5 and lmc8) and East of Madagascar (EMC1 and EMC3)

modulation of the harmonic constants, to the effect that the 'string of pearls'—the spring-neap tidal cycle—is retrieved also at mid-depth levels (see Fig. 4f–h). Other sites in the Mozambique Channel, further to the West, are more strongly affected by eddies, internal tides and blow-down of instruments. These mask the barotropic signal within the water column, and make the surface tide visible and reliably detectable near the sea bottom only.

Stratification

The ocean is a stratified medium, and so is the region on either side of Madagascar. Buoyancy frequency squared (N^2) profiles, were extracted for the regions of interest from the CSIRO Atlas of Regional Seas (CARS2009). This merges data from both research vessel instrument profiles and autonomous profiling (e.g., Argo floats), and is distributed on a 1/2° degree horizontal grid. For every grid point, the product also provides a correction for the annual cycle which allows users to create profiles for any date/season of the year. Figure 16 shows four typical N^2-profiles on either side of Madagascar. Both regions are characterised by a strong, shallow (seasonal) pycnocline (with a sharp maximum at a depth of about 50m, especially at EMC1). EM displayed also a deeper, second permanent pycnocline, at 850 m depth. Both

density profiles are stably-stratified down to the bottom, thus allowing for internal tides to propagate.

Mozambique Channel Coherent Internal Tides

Internal tides are ubiquitous [25], and in the Indian Ocean reach vertical amplitudes of 80 m or more, especially near Mascarene Ridge, close to the Seychelles (Fig. 2), to the North-East of Madagascar [16, 25]. There, internal tides take the shape of solitons, having large vertical isopycnal excursions of O (100 m), that find marked surface expressions [9]. In Mozambique Channel, internal solitons have also been observed south of our transect, near Sofala bank at 20.5° S where tides are stronger than in the MC narrows [8]. The clear patterns of waves in their satellite observations have been attributed to horizontally-propagating solitons, trapped to the pycnocline, that were generated either at the shelf edge or by upward-propagating internal wave beams impinging on the seasonal pycnocline from below. The latter beam itself was identified as the bottom reflection of a previously downward-propagating internal wave beam that was also produced at the shelf edge.

Along our Mozambique Channel transect, indications of mainly incoherent tides were extracted from ADCP and current meter records during the Agulhas Current Source EXperiment (ACSEX), a precursor of the LOCO projects used in the present study [23]. That study shows the internal tides to be quite intermittent. Their spatial structure, however, seems to accord with internal tides taking the shape of relatively broad beams, O (100 km) wide, also found in their numerical model. These beams follow nearly parabolic paths owing to the decrease in buoyancy frequency with increasing depth and corresponding steepening of internal wave paths, seen in Fig. 16.

In the present study, BPR-derived harmonic amplitudes and phases are the only ones that can confidently be attributed to surface tides. The magnitude of the coherent internal tides, displayed in Fig. 17, were obtained by subtracting these BPR-derived surface tidal harmonic vectors. As the semidiurnal surface tide is much larger, O (113 cm), than the coherent internal tide, having 'equivalent surface displacements' O (8 cm), only the surface tidal harmonic vector directions are shown in this figure (black sticks), their magnitudes, A_{surf}, being listed in each panel's legend. Recall that the apparently small magnitudes of the coherent internal tidal vectors represent a pressure perturbation, here expressed as an equivalent surface displacement, that can also be interpreted as a much larger internal, isopycnal displacement. The latter will magnify the surface displacement, crudely speaking by a factor δ^{-1}. For δ of O (10^{-3}), this brings us back to an estimated internal isopycnal displacement of O (80 m), as reported above for solitary wave displacements in the region.

One outstanding feature is the coherency of the surface tide along the Channel cross-section (different rows), a feature already addressed in section "Coherent Surface and Internal Tides". As mentioned, the coherent internal tides in Figs. 17 and 18 (coloured vectors) are obtained by subtracting at each level the surface tide

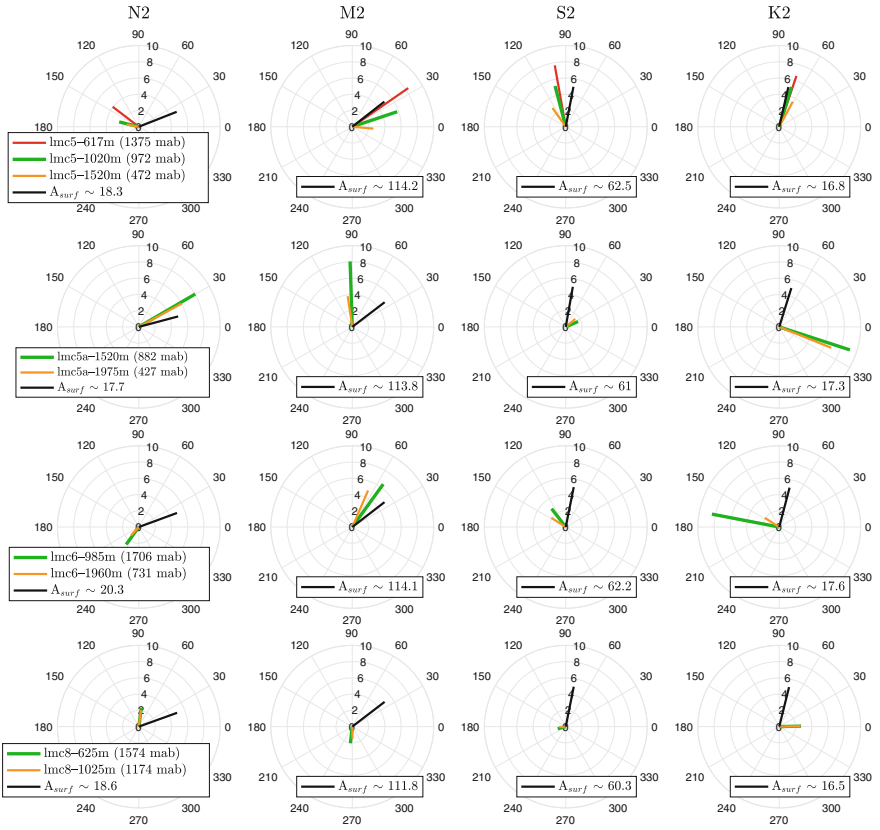

Fig. 17 Vertical variation of MC amplitudes (cm) and phases (°) of displacements by semidiurnal tidal constituents at sites arranged in rows from West (lmc5, top row), via the Middle (lmc5a and lmc6) to East (lmc8, bottom row). Coloured bars represent *coherent internal* tides. Black bar gives *direction* of surface tide (as measured at bottom). Amplitude of the surface tide, A_{surf}, is given in the legend (see Table 6 for further details). From left to right, columns represent tidal constituents N2, M2, S2 and K2, respectively. Here polar plots share the same scale only within the same column, i.e. tidal constituent

(Table 6) from the original harmonic vectors, i.e. the MT_TIDE average of the curves shown in Figs. 6 and 7. The existence of similar long-term, phase-locked internal tides were for instance observed near Hawaii [35]. The phase differences with depth that one obtains along a mooring in the vertical show direct evidence of oblique—beam-wise—internal tide propagation. In continuously-stratified fluids, upward phase propagation of internal waves (such as seen for M2 at lmc5) corresponds to downward energy propagation. Notice that at other locations (e.g. at lmc6) for M2, the phase decreases from the bottom upwards. Hence it displays a downward phase and upward energy propagation. Apparently, part of the multiply-reflected internal tidal beam is captured. Phase equality over depth (such as for all

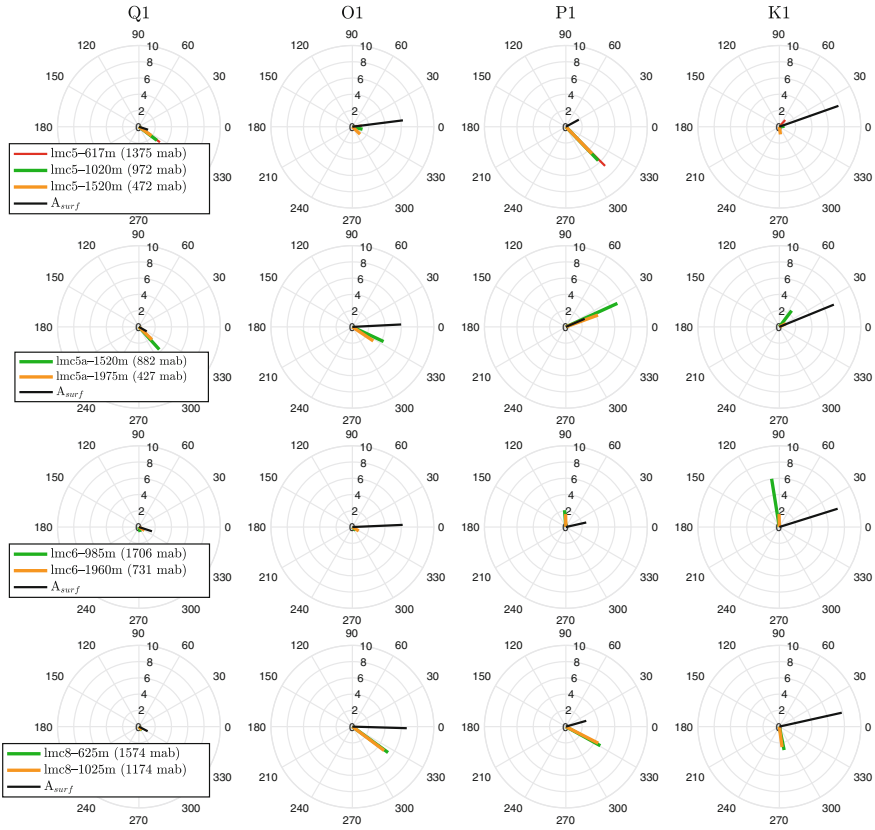

Fig. 18 As Fig. 17 for diurnal frequencies, from left to right: Q1, O1, P1 and K1, respectively, except that surface tidal amplitude (A_{surf}, black bar) here corresponds to bar length

frequencies at lmc5a and lmc8) implies either dominance of the surface tide or a horizontally-propagating, coherent internal tide. However, one has to keep in mind the very small aspect ratio of MC, and the ocean in general, so that low-frequency internal tides propagate at very small angles to the horizontal. Phase differences of baroclinic tides that occur in transverse channel direction (seen along columns in Figs. 17 and 18) are indicative of their shorter length scales.

Looking at the coloured vectors in Fig. 17, one notices the overall variability in amplitude and phase of the internal tide harmonic vectors, although it seems they are strongest in the center of the Mozambique Channel, near lmc5, lmc5a and lmc6. It is also remarkable that the coherent internal K2 tide seems to be at least as strong as the coherent internal M2 tide, despite the free surface K2 tide being seven times weaker than the surface M2 tide.

Figure 18 shows the diurnal surface (black vectors) and internal tides (coloured). In this case, since amplitudes of the surface and internal tides lie in the same range, the surface tide's vector length corresponds its magnitude.

A remarkable property of these observations is that diurnal baroclinic tidal vertical displacements always seem stronger and sometimes much stronger than those produced by the surface tide, see e.g. in Fig. 18 the amplitude increases with increasing height above the bottom at lmc5 and lmc5a for frequencies Q1 and P1. This requires an amplification mechanism. This may be because internal tides, forced by cross-isobath surface tidal motions near the shelf edges of the adjacent coasts are focused near the center of the Mozambique Channel. At the shelf edge, its amplitude will be set by the local surface tide, which, due to a reduced shelf depth, will be stronger than over the deep-sea, hence leading to stronger internal tides. Another reason for elevated amplitude levels of internal tides may be that once internal tides propagate beam-wise into the abyss, they reflect from sloping bottoms, at which point they will often be focused, leading to amplification of their energy density.

It is also remarkable that nearly all diurnal internal tide vectors are co-aligned with one another. This means they are in phase, with vectors increasing in magnitude higher up in the water column. This suggests them to be propagating horizontally, varying in magnitude along the vertical.

East Madagascar Coherent Internal Tides

For EM moorings we do not have collocated bottom and mid-depth instruments. Therefore, estimates from mid-depth instruments might contain the signal of both surface and internal tides. In Fig. 13, the harmonic vectors within the water column, at EMC2, 4 and 5, however, dwarf those at EMC1 and 3, related to the surface tide at the bottom. Evidently coherent internal tides are remarkably strong on the transect East of Madagascar. Looking at the semidiurnal components (lowest two rows), curiously, tidal phases within the water column are generally in opposition to those of the surface tide (as measured by BPRs). Even though moorings are up to 100 km apart, for the M2-tide the phase relationship within the water column is very tight. Subtracting the surface M2 tide (measured at EMC3 or OTIS) by eye from the harmonic vectors within the water column, leads to equivalent surface displacements due to internal tides of O (50 cm). With the conversion employed in section "Mozambique Channel Coherent Internal Tides" this would suggest isopycnal displacements of O(500 m)! Such large magnitude is suspicious and should be treated with caution. It is quite unexpected because of the weakness of the surface tide along the EM transect and surroundings. Near sloping topography, surface and coherent internal tides are not necessarily scale separated [22, 43]. This suggests the internal tide to have a barotropic length scale, such as for a forced internal tide. For S2 there appear some horizontal phase differences, suggesting the S2 coherent internal tide to have a propagating character.

Incoherent Internal Tides

So far we have discussed the surface tides (based on BPRs, section "Bottom-Pressure Versus Altimetry Derived Tides") and the coherent internal tides (which are long-period averages from MT_TIDE). For this, in MC we first subtracted the surface tide (section "Mozambique Channel Coherent Internal Tides"), while in EM the surface tide is much smaller than the coherent internal tide so that the long-period average immediately give an estimate for the coherent internal tides (section "East Madagascar Coherent Internal Tides"). Figures 6, 7, 8, 9, 10 and 11, however, also show large variations of tidal amplitudes and phases around their averages. These represent *incoherent* internal tides. These can, crudely speaking, be of comparable magnitude as the coherent internal tide. The large, mid-water column tidal amplitudes in e.g. Fig. 8 display gradual as well as sudden changes. The sudden jumps might be related to large-scale (blow-down) events, despite the applied filters. The data gaps that have been replacing these events, that enter or leave the analysed one-year time interval, may still have a disruptive effect. We notice that such jumps do not occur for the bottom instrument. The mid water-column pressure records at lmc5a are remarkable in showing correlating drops in M2, S2, K2 and P1 amplitudes, taking place from February to July 2013. This drop below the average levels given in Table 6 suggests that internal tides at instrument levels more than 425 m above the bottom have a significant presence during these periods. Notice that such internal tide variations also showed up in the mid water column pressure records of Figs. 6 and 7. N2, M2 and S2 amplitudes, as well as K2 phases, suggest the internal tides at lmc5a to be often anti-correlated with those at lmc6, their values fluctuating around those representative of the surface tide. This change in internal tide amplitude on relatively nearby moorings suggests that internal tidal beams change path due to variations in mean density and flow fields.

Conclusions

New bottom pressure records for the South-West Indian Ocean have been presented. These can be reliably interpreted as providing measurements of the surface tides and compare in general well with the satellite altimetry derived tides. As such, these BPRs might be useful in future world-wide assimilation of deep pressure data in numerical models of ocean tides when combined with altimetric data. According to Ray's [34] separation criteria, the moorings may not be separated well enough (by about 100 km) to be treated as independent, so that MC and EM transects may deliver two independent data points only. At the same time, spatial variations in BPRs in the vicinity of the coast may be realistic, and may prompt the development of a better resolution in near-coastal altimetry measurements.

Pressure measurements within the water column regularly suffer from blow-down of moorings by eddy, buoyancy, tidal and wind-driven flows. Blow-down leads to

virtual excursions much in excess of those realistically possible. These affect also the estimates of (internal) tides, due to tidal currents amplifying this blow-down—an unwanted effect—or due to trapping of internal tides within eddies, which we have not been able to unravel here. Accordingly, we simply eliminated blow-down events. In future work, one could compute actual instrument displacements using observed currents along the moorings, combined with a knowledge on the shape of the mooring line, the weights of instruments and cable, and the buoy's shape, size and buoyancy [11].

The reason to nevertheless study mid water-column pressure is the presence of both coherent as well as incoherent (i.e. intermittent) internal tides [23]. Intermittency is due to the varying paths taken by internal tides from generation sites (near shelf edges and other bottom irregularities, at critically sloping bathymetry) to measurement locations. These paths vary due to slow changes in density and velocity fields, associated with low-frequency motions.

Performing harmonic analysis (T_TIDE) over consecutive overlapping intervals we obtained multiple estimates of harmonic amplitudes and phases (MT_TIDE). The coherent surface and internal tidal constants are independent of the measurement period and are thus represented by the average of MT_TIDE. The variable part defines the incoherent internal tide. This allows separation of the coherent and incoherent tides (determined by their robustness and variance, respectively) in a manner that may be more reliable than the error band provided by T_TIDE from a single (year long) time series [28].

Both the coherent as well as incoherent tides are fairly strong, especially when the equivalent surface displacement is reconverted into isopycnal displacement. The latter can attain excursions of tens to hundreds of meters. The phase variation of the coherent and incoherent internal tides along a mooring line is usually weak. The amplitude variations are stronger. Horizontal variations are, obviously much larger, clearly displaying an internal tidal length scale that is much shorter than that of the corresponding surface tide.

Acknowledgements This work is dedicated to Eugene Morozov on the occasion of his seventieth birthday. The authors are thankful to Gary Egbert, Lana Erofeeva and Oregon State University for providing the altimetry-derived barotropic tides and to the Royal Netherlands Institute for Sea Research for providing the pressure data. Pressure data were collected in the INATEX program, 'INdian-ATlantic EXchange in present and past climate', funded by the Netherlands Organization for Scientific Research (NWO), section Earth and Life Sciences (ALW), through its ZKO Grant 839.08.43. The authors acknowledge Commonwealth Scientific and Industrial Research Organisation (CSIRO) for making available the Atlas of Regional Seas 2009 (CARS2009).

References

1. Alford, M. H. (2003). Redistribution of energy available for ocean mixing by long-range propagation of internal waves. *Nature*, *423*, 159–162.

2. Badulin, S. I., Shrira, V. I., & Tsimring, L. S. (1985). The trapping and vertical focusing of internal waves in a pycnocline due to the horizontal inhomogeneities of density and currents. *Journal of Fluid Mechanics*, *158*, 199–218.
3. Berry, M. (1987). The Bakerian lecture 1987: quantum chaology. *Proceedings of the Royal Society of London A*, *413*, 183–198.
4. Bewley, G. P., Lathrop, D. P., Maas, L. R. M., & Sreenivasan, K. R. (2007). Inertial waves in rotating grid turbulence. *Physics of Fluids*, *19*(7), 071701.
5. Boisson, J., Lamriben, C., Maas, L. R. M., Cortet, P. P., & Moisy, F. (2012). Inertial waves and modes excited by the libration of a rotating cube. *Physics of Fluids*, *24*(7), 076602.
6. Cartwright, D. E. (2000). *Tides: A scientific history*. Cambridge: Cambridge University Press.
7. Cartwright, D. E., & Ray, R. D. (1990). Oceanic tides from Geosat altimetry. *Journal of Geophysical Research: Oceans*, *95*(C3), 3069–3090.
8. da Silva, J. C. B., New, A. L., & Magalhães, J. M. (2009). Internal solitary waves in the Mozambique Channel: observations and interpretation. *Journal of Geophysical Research*, *114*, C05001. https://doi.org/10.1029/2008JC005125.
9. da Silva, J. C. B., New, A. L., & Magalhães, J. (2011). On the structure and propagation of internal solitary waves generated at the Mascarene Plateau in the Indian Ocean. *Deep-Sea Research I*, *58*, 229–240.
10. Defant, A. (1961). *Physical oceanography* (Vol. 2).
11. Dewey, R. K. (1999). Mooring design and dynamics: A Matlab package for designing and analyzing oceanographic moorings. *Marine Models*, *1*(1), 103–157.
12. Egbert, G. D., & Erofeeva, S. Y. (2002). Efficient inverse modeling of barotropic ocean tides. *Journal of Atmospheric and Oceanic Technology*, *19*, 183–204.
13. Harlander, U., Ridderinkhof, H., Schouten, M. W. & de Ruijter, W. P. M. (2009). Long-term observations of transport, eddies, and Rossby waves in the Mozambique Channel, *Journal of Geophysical Research*, *114*(C02003), 1–15.
14. Hendershott, M. C. (1981). Long waves and ocean tides. In *Evolution of physical oceanography* (pp. 292–341).
15. Hutter, K., Wang, Y., & Chubarenko, I. P. (2011). *Physics of lakes*. Springer.
16. Konyaev, K. V., Sabinin, K. D., & Serebryany, A. N. (1995). Large-amplitude internal waves at the Mascarene Ridge in the Indian Ocean. *Deep Sea Research Part I: Oceanographic Research Papers*, *42*(11–12), 20752083–20812091.
17. Kunze, E. (1985). Near-inertial wave propagation in geostrophic shear. *Journal of Physical Oceanography*, *15*, 544–565.
18. Lamriben, C., Cortet, P. P., Moisy, F., & Maas, L. R. M. (2011). Excitation of inertial modes in a closed grid turbulence experiment under rotation. *Physics of Fluids*, *23*(1), 015102.
19. LeBlond, P. H., & Mysak, L. A. (1981). *Waves in the ocean*. Elsevier.
20. Maas, L. R. M. (1997). On the nonlinear Helmholtz response of almost-enclosed tidal basins with sloping bottoms. *Journal of Fluid Mechanics*, *349*, 361–380.
21. Maas, L. R. M. (2003). On the amphidromic structure of inertial waves in a rectangular parallelepiped. *Fluid Dynamics Research*, *33*, 373–401.
22. Maas, L. R. M. (2011). Topographies lacking tidal conversion. *Journal of Fluid Mechanics*, *684*, 5–24.
23. Manders, A. M. M., Maas, L. R. M., & Gerkema, T. (2004). Observations of internal tides in the Mozambique Channel. *Journal of Geophysical Research: Oceans*, *109*(C12).
24. Moum, J. N., & Nash, J. D. (2008). Seafloor pressure measurements of nonlinear internal waves. *Journal of Physical Oceanography*, *38*(2), 481–491.
25. Morozov, E. G. (1995). Semidiurnal internal wave global field. *Deep Sea Research Part I: Oceanographic Research Papers*, *42*(1), 135–148.
26. Munk, W. H., & Cartwright, D. E. (1966). Tidal spectroscopy and prediction. *Philosophical Transactions of the Royal Society of London*, *259*(1105), 533–581.
27. Nurijanyan, S., Bokhove, O., & Maas, L. R. M. (2013). A new semi-analytical solution for inertial waves in a rectangular parallelepiped. *Physics of Fluids*, *25*(12), 126601.

28. Pawlowicz, R., Beardsley, B., & Lentz, S. (2002). Classical tidal harmonic analysis including error estimates in MATLAB using T_TIDE. *Computers and Geosciences*, *28*(8), 929–937.
29. Platzman, G. W. (1971). Ocean tides and related waves. *Mathematical Problems in the Geophysical Sciences*, 14(Part 2), 239–291.
30. Ponsoni, L., Aguiar-González, B., Maas, L. R. M., van Aken, H. M., & Ridderinkhof, H. (2015). Long-term observations of the East Madagascar Undercurrent. *Deep-Sea Research I*, *100*, 64–78.
31. Ponsoni, L., Aguiar-González, B., Ridderinkhof, H., & Maas, L. R. M. (2016). The East Madagascar Current: Volume transport and variability based on long-term observations. *Journal of Physical Oceanography*, *46*(4), 1045–1065.
32. Proudman, J. (1917). On the dynamic equation of the tides. Parts 1–3. *Proceedings of the London Mathematical Society*, Series 2, *18*, 168.
33. Rao, D. (1966). Free gravitational oscillations in rotating rectangular basins. *Journal of Fluid Mechanics*, *25*, 523–555.
34. Ray, R. D. (2013). Precise comparisons of bottom-pressure and altimetric ocean tides. *Journal of Geophysical Research: Oceans*, *118*(9), 4570–4584.
35. Ray, R. D., & Mitchum, G. T. (1997). Surface manifestation of internal tides in the deep ocean: Observations from altimetry and island gauges. *Progress in Oceanography*, 35–162.
36. Ridderinkhof, H., van der Werf, P. M., Ullgren, J. E., van Aken, H. M., van Leeuwen, P. J. & de Ruijter, W. P. M. (2010). Seasonal and interannual variability in the Mozambique Channel from moored current observations. *Journal of Geophysical Research: Oceans*, *115*(C06010), 1–18.
37. Schrama, E. J. O., & Ray, R. D. (1994). A preliminary tidal analysis of TOPEX/POSEIDON altimetry. *Journal of Geophysical Research: Oceans*, *99*(C12), 24799–24808.
38. Taylor, G. I. (1921). Tidal oscillations in gulfs and basins. *Proceedings of the London Mathematical Society*, Series 2, 148–181.
39. Terra, G. M., Doelman, A., & Maas, L. R. (2004). Weakly nonlinear cubic interactions in coastal resonance. *Journal of Fluid Mechanics*, *520*, 93–134.
40. Ullgren, J. E., van Aken, H. M., Ridderinkhof, H., & de Ruijter, W. P. M. (2012). The hydrography of the Mozambique Channel from six years of continuous temperature, salinity, and velocity observations. *Deep Sea Research Part I: Oceanographic Research Papers*, *69*, 36–50.
41. van Haren, H. (2013). Bottom-pressure observations of deep-sea internal hydrostatic and non-hydrostatic motions. *Journal of Fluid Mechanics*, *714*, 591–611.
42. Whewell, W. (1836). Researches on the tides. Sixth series. On the results of an extensive system of tide observations made on the coasts of Europe and America in June 1835. *Phillosophical Transactions of the Royal Society of London*, *126*, 289–341.
43. Zaron, E. D. & Egbert, G. D. (2007). The impact of the M2 internal tide on data-assimilative model estimates of the surface tide. *Ocean Modelling*, *18*, 210–216.